NOVEL POLYMER-DERIVED CERAMIC ANTENNAS FOR HYPERSONIC APPLICATIONS

A Thesis Presented for the

Master of Science

Degree

The University of Tennessee, Knoxville

Peter Jessup Alley

August 2024

ACKNOWLEGEMENTS

I would like to thank Dr. Aly E. Fathy, Dr. Brett G. Compton, and Dr. Benjamin J. Blalock for agreeing to be on my committee.

To Dr. Fathy, thank you for letting me to take up residency in his Microwave Research Group (both figuratively, and somewhat literally), for all the expertise and wisdom he provided both in is lectures, and advisory role; and for generously tolerating my often-unconventional approaches to problem solving and research.

To Dr. Compton, and Dr. Robert C. Pack, thank you for allowing me to take part in this phenomenal project, and providing your expertise and knowledge across all mechanical and material aspects of it which I decisively lacked. Additional shoutout to Dr. Pack for his masterful milling skills, and repeatedly staying late to help me with testing. It has been a pleasure working with both of you.

To Dr. Benjamin J. Blalock, thank you for keeping the art of analog electronic design alive and flourishing for generations to come. It’s been an honor and a privilege to serve as GTA for your courses over the years (shoutout to the students as well).

To everyone from the Microwave Research Group: Abdel-Kareem Moadi, Chandler Bauder, Marvin Joshi; Thank you for all your help, advice, and expertise. You have made the lab a very enjoyable place to work, and have had a lasting impact on my sanity (for better or worse).

I’d also like to thank the former members of the Student Space Technology Association (SSTA), particularly Peter Tarlé, Robert Nickel, Alex Allen, and Dr. James E. Lyne (Aerospace Engineering department) for their part in helping me learn the underlying concepts of rocketry, propulsion, and (most notably) hypersonics.

PREFACE

The investigation described in this thesis was part of a 2-year research project championed by PI Dr. Brett Compton and post-Doc Dr. Robert Pack, Mechanical Engineering Department, University of Tennessee, with funding provided by Lockheed-Martin. The novel PDC materials/formulations, 3D-printing, and fabrication processes used are of Dr. Compton's and Dr. Pack's original creation; developed during the first year.

At the beginning of year two, they reached out to Dr. Aly Fathy, Electrical Engineering Department, University of Tennessee, seeking help from his Microwave Research Group in designing and testing antennas using their creations. The author of this thesis, having a "casual" background in rocketry due to his years-long prior involvement in the Student Space Technology Association (SSTA), and possessing a level-two amateur rocketry certification, was selected from the Microwave Group to take on this endeavor.

ABSTRACT

With recent advances in three-dimensional [3D] printing of polymer-derived ceramics [PDCs], and the controllability of electrical continuity thereof, interest has risen in potential applications resultant from these techniques in the realm of radio communication, particularly in cases where extreme high temperatures are ambient. The following investigates the electrical properties of both insulating and conductive variants of these PDCs, the interaction between each, and the performance characteristics observed when combined using microstrip antenna design theory for high temperature applications.

TABLE OF CONTENTS

CHAPTER I: OVERVIEW 1
1.1 Background 1
1.2 Hypersonics 2
1.3 Scope of Thesis 5
CHAPTER II: DIELECTRIC CHARACTERIZATION 7
2.1 Introduction 7
2.2 Dielectric Theory 7
2.3 Methods of Characterization 11
CHAPTER III: MATERIAL CHARACTERIZATION AND PROTOTYPING . . . 18
3.1 Background 18
3.2 hBN Preliminary Samples 20
3.3 Open-ended Coaxial Probe Measurements 22
3.4 Transmission Line Measurements 23
3.5 Resonant Patch Antenna Design 26
CHAPTER IV: HIGH TEMPERATURE ANTENNA TESTING 40
4.1 Background 40
4.2 High Temp. Testing – Logistical Considerations 41
4.3 Furnace Tests 48
4.4 Torch Tests 54
4.5 Torch Test Procedure 64
CHAPTER V: TORCH TEST RESULTS AND DISCUSSION 66
5.1 Color Commentary 66
5.2 Consolidated Results Analysis 77
CHAPTER VI: CONCLUSION 83
6.1 Summary 83
6.2 Conclusions 84
6.3 Future Works 85
REFERENCES 87
APPENDIX 88
VITA 91

LIST OF FIGURES

Figure 2.1 Vectors of Dielectric Permittivity 10
Figure 2.2 Summary of Dielectric Characterization Methods . 12
Figure 3.1 Fabrication Process Flow 19
Figure 3.2 Dual-Nozzle Pressure-fed 3D Printing Process . . 19
Figure 3.3 hBN Samples 21
Figure 3.4 HP 85070B Dielectric Probe 21
Figure 3.5 Dielectric Measurements of Preliminary Samples . 24
Figure 3.6 Avg Dielectric Const vs Freq - Prelim Samples . 24
Figure 3.7 Copper Transmission Line, PCAAD Model 25
Figure 3.8 ADS Simulation Model – Copper Line 27
Figure 3.9 CST Model – Lateral-fed Patch Antenna 29
Figure 3.10 First Prototype Batch – Lateral-fed Patch . . . 29
Figure 3.11 Improved Coupling – Silver Epoxy 30
Figure 3.12 Reflection Measurements – First Batch Antennas . 32
Figure 3.13 First Batch Prototypes & Farfield Plots . . . 32-33
Figure 3.14 PCAAD Model – Probe-fed Patch Antenna 33
Figure 3.15 Cross-sectional view of Patch Antenna 35
Figure 3.16 Batch-2 Antennas 35
Figure 3.17 Reflection and Farfield plots – Batch-2 Antennas 36
Figure 3.18 Copper Tape Resonance Tuning 38
Figure 3.19 CST Dielectric Constant Parameter Sweep 38
Figure 3.20 CST Simulation/Measurement Comparisons 39
Figure 4.1 High Temperature Coaxial Feed Line 42
Figure 4.2 Open ‘Hot’ End of Feed Line 42
Figure 4.3 Aremco High Temperature Silver Epoxy 42
Figure 4.4 Cross Section of HT Feed Line Connection 44
Figure 4.5 Antenna-to-Feed Line Mounting Process 44
Figure 4.6 High Temperature Feed Line – Reference Line . . 44
Figure 4.7 Reference Line Measurement 46-47
Figure 4.8 Barnstead Thermolyne 47900 Furnace 50
Figure 4.9 Furnace Test Diagram & Apparatus 50
Figure 4.10 500C Furnace Test Measurements 52
Figure 4.11 Furnace Test at 900C 52
Figure 4.12 Antenna Aftermath & Plots – 900C Furnace Test . 52
Figure 4.13 S11 Measurements – 900C Furnace Test 53
Figure 4.14 Signal Flow Diagram – Network Analyzer 57
Figure 4.15 12-Term Error Correction Diagram 57
Figure 4.16 Torch Test Apparatus 61-63
Figure 5.1 Frames from Notable Events – Torch Test Video 70-76
Figure 5.2 Consolidated Telemetry Extrema Plots 78-79

CHAPTER I

OVERVIEW

1.1 Background

Wireless communication and guidance has been an all but ubiquitous facet of both aeronautics and astronautics. Historically, the primary concerns regarding implementation merely consisted of transmit power, weight, and spatial constraints. At higher speeds, dopier shift effects need to be addressed as well. Antennas serve as the categorical terminus of any radio system. While much consideration is already required concerning their designs with respect to frequency, bandwidth, directivity, and gain; Their integration into aerospace vehicles and vessels poses an additional litany of challenges.

Properly designed airframes feature smooth exteriors and a profile whose cross section normal to the direction of movement is minimal. A dichotomy quickly emerges between those tenants and that of proper design and Installation of any/all antennas. Idea11y, the antennas would need to be mounted on the exterior of the airframe to obtain an unobstructed signal path between their resonant elements and those of the remote transmit/receive antennas. Such placement limits many of the antenna's design freedoms as its physical shape will need to conform to that of the surrounding structure as to not impede upon the airframe's aerodynamic characteristics.

While the measures one may take in order to incorporate an antenna into the exterior of an airframe (without drastically

compromising the performance of either) can pose a bit of an undertaking, this difficulty is compounded exponentially when everything is literally on fire. Such is the precipice of hypersonics.

1.2 Hypersonics

An object is typically considered to be traveling at hypersonic velocity when it exceeds Mach 5. This threshold, however, lacks nuance. For one, much like the generalized threshold for mere supersonic speeds, it is entirely dependent on the speed of sound, which itself is not a constant. The density and temperature of the given medium; be it air, water, etc. all play a deterministic role as to its speed of sound at any given moment.

Its motion relative to both an external observer and/or any object traversing through it is also a factor. In instances where the elastic medium is more-or—less nonexistent (i.e.: the vacuum of space), the "speed of sound" is, while still technically present within the probabilistic domain of ultra—low density particles interacting with each other, functionally irrelevant with respect to macroscopic objects traversing through it (save for collective effects of drag). Thus, for orbital vessels such as the International Space Station (ISS), while it technically orbits at approximately Mach 20, and would therefore be handedly transcendent of the “Mach 5” hypersonic threshold, it would not be an accurate assertion to classify it as traveling hypersonically. A more accurate characterization of the ISS's speed is that of “hypervelocity, in a rarified environment”.

Should it encounter an atmosphere of sufficient density at those speeds, however, only then may it be considered hypersonic.

A defining attribute of hypersonic transit that provides a much more precise benchmark is that of heat transference. At hypersonic speeds, the rate at which heat generated as result of friction and/or bombardment of the air/medium against the prevailing surfaces of the object traversing through it, is higher than the rate at which it dissipates. Thus, the heating is effectively exponential. Should the object endure indefinite hypersonic transit, its exposed surface will inevitably be heated beyond its material limit in short order, at which point (regardless of the material) it will begin to disintegrate on a molecular level; being ejected from the object in the form of plasma.

For vehicles constructed to both withstand, and sustain prolonged* passages at hypersonic speeds, a sacrificial ablative material is used to line the prevailing exterior surfaces of the vehicle. This material conforms to the airframe's surface in order to maintain the structure's desired aerodynamic characteristics but is able to "burn away" in a uniform manner, dissipating heat in the process throughout the duration of transit.

Two primary methods of sacrificial material cooling are ablative solid panels (typically phenolic) and fluid film cooling. Ablative

* While relatively-long durations are possible. Durability is inherently temporary, depending on ablative material rate of regression.

panels act as the outer surface of the airframe throughout the entire flight, including prior to, and (of what remains) following the transitions into and out of hypersonic transit. These panels/tiles must be replaced prior to successive excursions depending on wear. Fluid film cooling consists of a gas or liquid that is extruded through perforations across the airframe's surface.

An immediate advantage of film cooling is the relative ease of replenishment, compared to ablative tile replacement. Other benefits include the controllability of the cooling in a dynamic manner, as well as the ability of the airframe to retain a more permanent outer surface, unburdened by inherent material loss, and in turn, able to be composed of non-ablative (yet still thermally rugged) materials. It should also be of note that in most instances, provided that the leading-edge surfaces of a vehicle's airframe have sufficient cooling, any/all trailing surfaces will typically not require such sacrificial material cooling schemes, and instead need only be composed of materials robust such to withstand the residual heat.

Despite the advancements made to harden an airframe against the environmental extremes involved in hypersonic flight, the incorporation of antennas into the framework has largely remained a dubious endeavor. The primary hindrance is that of an antenna's inherent fragility, due to a combination of root necessities, including electrically conductive materials, geometric complexity and precision. Traditionally, the workaround approach is to either relegate placement of the antenna to the aft of the vehicle or recess the antenna behind a sufficient shield. Either

approach will tend to result in greatly diminished performance (in some instances, complete inoperability for the duration of hypersonic transit), and/or greatly increased cost and complexity.

Recent innovations in the field of material development and manufacturing; specifica11y those of conductive additive formulation for polymer derived ceramics (PDCs), and 3D printing techniques that are compatible with PDCs, offer a plethora of opportunities for antenna development in hypersonic applications.

1.3 Scope of Thesis

The purpose of this thesis is to investigate the viability of newly—developed co—fired pre-ceramic polymers, to be used in place of conventional metal and insulative substrate materials in the creation of functional antennas, constructed via a novel 3D-printing technique, that are thermally robust to the magnitude of temperatures typically experienced during hypersonic transit. The thesis will be limited to a singular microstrip patch antenna form factor such to evenly test the characteristics of both conductive and insulative material formulations.

The goals of this thesis are to (1) characterize the PDC formulations' dielectric properties, (2) design a rectangular microstrip patch antenna based on the findings from dielectric characterization, (3) evaluate and refine both design and manufacturing process, (4) produce a functional prototype antenna that yields (5) positive gain, and (6) test its performance and robustness at temperatures up to 900°C.

Given both the novelty of materials and manufacturing techniques, as well as the inherent national security concerns ubiquitously synonymous with that of hypersonic technology, unclassified published work on this specific area is scarce. This is further compounded by the prospects of radio-based communication, guidance, and radar applications; all of which are heavily the subject of proprietary confidentiality in the private sector, with a blanket of export control looming above.

Chapter II presents an evaluation of dielectric characterization techniques. Chapter III details the characterization of the novel PDC formulations, evaluation of manufacturing technique, antenna design, prototyping, testing. and refinement. Chapter IV details an exploratory approach to formulating and implementing a strategy for high temperature antenna testing. The experimental results are presented in Chapter V. Chapter VI contains a summary of research, conclusions, and future works.

CHAPTER II

DIELECTRIC CHARACTERIZATION

2.1 Introduction

The electrical properties of the substrate are critical to the design of microstrip circuits and resonators. They are the foundational parameters, from which all other aspects of the design are based around, in order to achieve optimal performance. It is very-much analogous to that of a car's suspension, consisting of both springs and shock absorbers. For a car to handle well, its suspension must properly complement the characteristics of the track it is driving around. From an electrical perspective, the substrate layer behaves similarly as it has both capacitance [springs] and loss [shocks] characteristics, and the 'track' can be compared to the frequency of intended operation. For this project, the substrate provided required a full gamut of characterization before a functional design could be produced.

2.2 Dielectric Theory

A dielectric material is electrically insulative in nature but has the ability to store energy from an externally applied electric field[1]. This is the fundamental principle that allows capacitors to operate. The amount of charge the dielectric material can hold per dimensional unit (area and thickness) is determined by its permittivity and permeability. The simplest model of these properties employs a "parallel plate" capacitor,

in which two flat conductive plates of known area and spacing are affixed to either side of a dielectric material of the same dimensional area and of thickness equal to the spacing between the plates. When a voltage is applied from one plate to the other, a certain amount of energy will enter the material, and a degree of electric displacement occurs. The electrodes will initially become neutralized as the material will behave as a conductor at first, but as the material reaches its full capacity, the electrodes will return to the same potential as before it was connected to the plates, and the material will 'go open' to the circuit.

The quantifiable amount of energy that enters, traverses, and/or stored in this manner is, in essence, normalized to a scenario in which nothing at all (e.g.: a hard vacuum) is between the plates. In such a 'no material' scenario, only free space permittivity [ε0], defined as a constant:

$$\varepsilon_0 \approx \frac{1}{36\pi} \times 10^{-9} \text{ F/m} \quad (1)$$

is in effect. The permittivity of all materials is referenced to this constant in the form of a ratio:

$$\varepsilon_r = \frac{\varepsilon}{\varepsilon_o} = K \quad (2)$$

Where ε_r is the material's relative permittivity, or dielectric constant [K]. ε_r is defined as a complex value $\varepsilon_r = \varepsilon' - j\varepsilon''$, where ε' (real part) represents the amount of energy able to be stored in the material, and ε'' represents the amount of loss or leakage through it. If one were to model these real/imaginary components along an X-Y plane where ε' is graphed along the X axis an ε'' is placed along the Y axis, a resultant vector is produced with an

angle δ rising from the ε' axis (see figure 2.1). For Insulators, $\varepsilon_r \approx \varepsilon'$ as excessive loss equates to non-negligible persistent conductivity.

A useful metric for determining the quality of a substrate's permittivity is the ratio between its dielectric constant and the real part of the constant's complex number, known as the material's loss tangent [TanD] or dissipation factor [D]. This ratio produces an inverse value to that of the material's quality factor [Q]:

$$\text{TanD} = \text{Tan}\,\delta = \frac{\varepsilon''}{\varepsilon'} = D = \frac{1}{Q} \tag{3}$$

Ideally, a substrate with the lowest dielectric constant and loss tangent is the best for high frequency microstrip design, however, of these two metrics, The substrate's loss tangent is the most critical to be as minimal as possible.

The translation in how a material's ε_r characteristics behave in regard to electromagnetism; we model it in the time domain to determine both its velocity factor and impedance. With respect to the speed of light [c] in free space [$c = 3 \times 10^8\, m/s$] The velocity factor [V_f] is defined as:

$$V_f = \frac{c}{\sqrt{\varepsilon r_r}} \tag{4}$$

And conversely:

$$\lambda_d = \frac{\lambda_0}{\sqrt{\varepsilon r_r}} \tag{5}$$

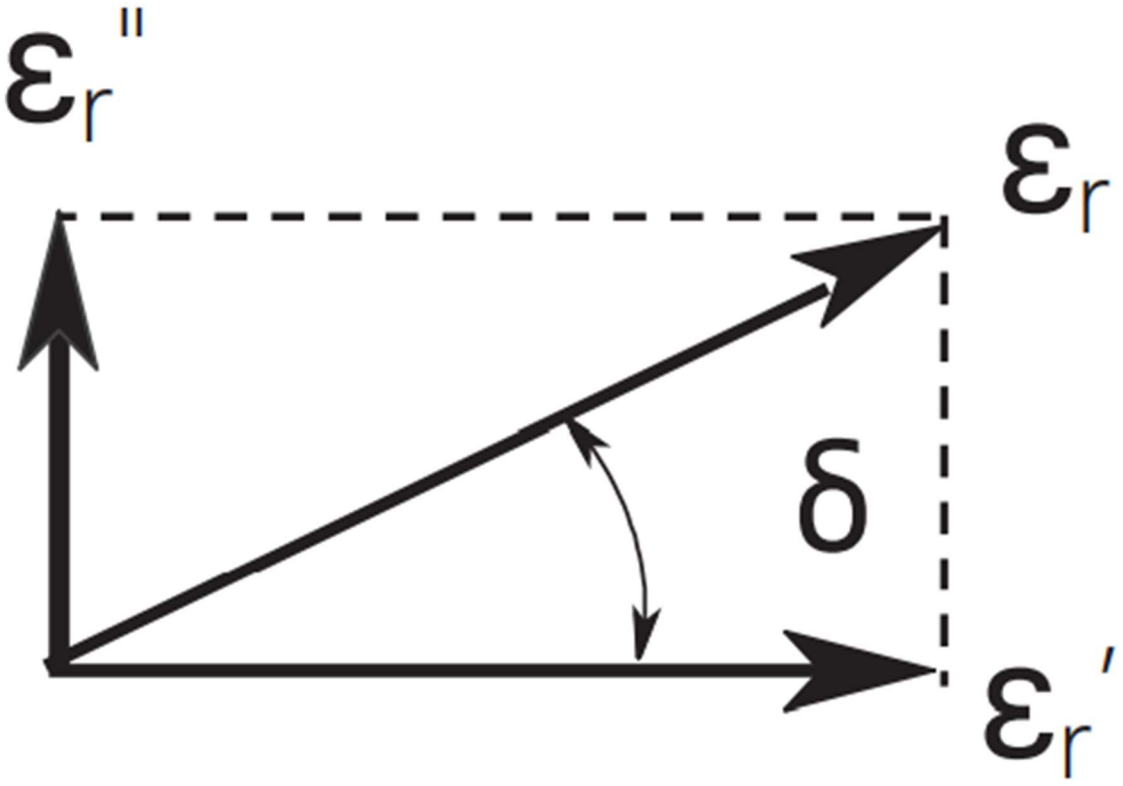


Figure 2.1: Vectors of Dielectric Permittivity[1]

Where λ_0 is the wavelength in free space and λ_d is the wavelength through the substrate. The impedance [Z] of the material is:

$$Z = \frac{Z_0}{\sqrt{\varepsilon_r}} \tag{6}$$

Where Z_0 is the free space impedance.

2.3 Methods of Characterization

Numerous techniques have been developed to measure the dielectric properties of various materials (Figure 2.2). These techniques each have their own sets of advantages and disadvantage. Selecting which technique(s) to use depends largely on the relevant frequency range of interest, and the material itself. As mentioned previously, the simplest measurement technique is that of the traditional parallel plate method. This technique is primarily useful for characterizing dielectric properties from DC to frequencies up to a few hundred megacycles, however, at higher frequencies, anomalies and fringe effects resultant from the more-or-less arbitrary geometry of the plates (relative to the frequency) can cause wide inaccuracies in the measurement.

For characterization at frequencies into the gigacycles, more attention must be given in how to go about transporting the test signal into and out of the material under test [MUT]. This is often addressed through the utilization of balanced transmission lines and coupling devices whose own electrical parasitics are both known and cancelable. The following is an overview of the most common techniques for measuring the dielectric constant at microwave frequencies:

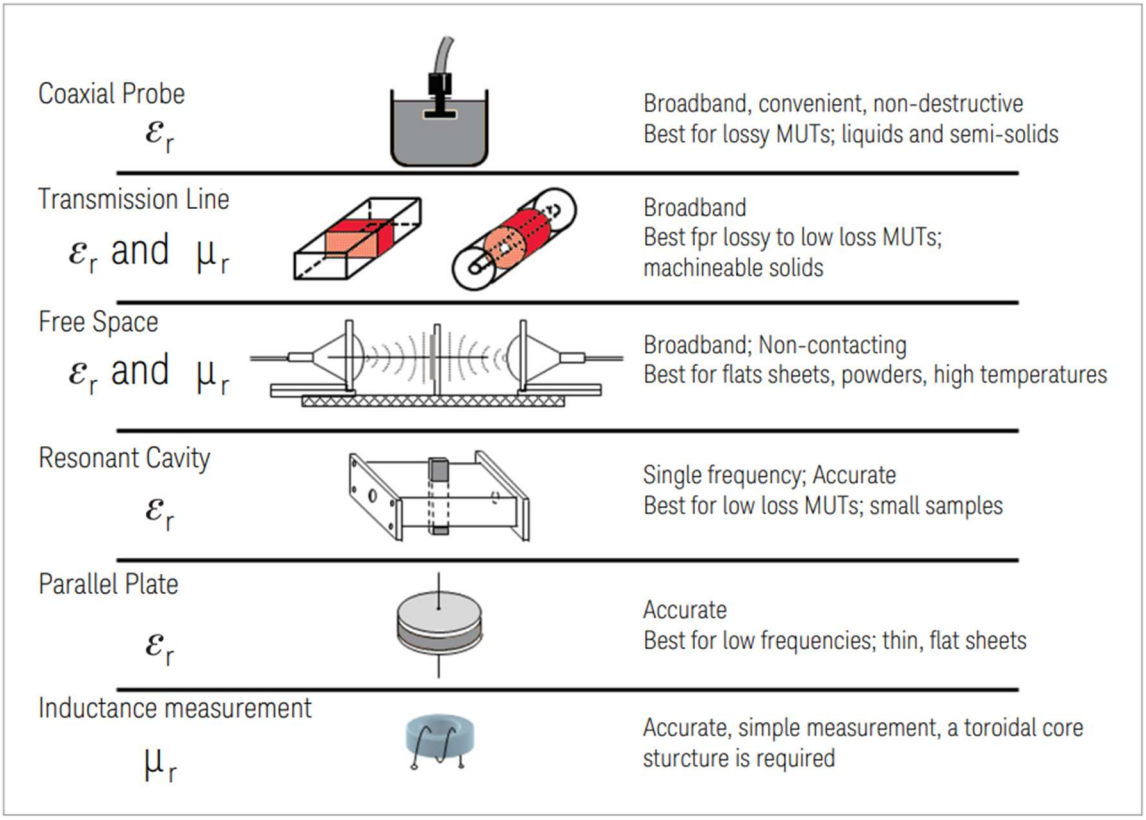


Figure 2.2: Summary of dielectric characterization methods[1]

1. Coaxial Probe: An open-ended coaxial transmission line featuring a wide metal flange for the outer conductor. The shape of this flange is key, as its face features a concentric recessed region (normal to the face) between the inner aperture and outer-most edge, creating a well-defined air gap (less than 0.5mm). This geometry is such that when the probe is submerged in room temperature water, it behaves as a balanced termination.
    - Advantage: This method allows for a network analyzer to normalize to this probe using a form of the conventional open-short-load (OSL) method of single port reflection calibration. The coaxial probe method is well-suited for measurements well into the tens of Gigacycles and can be used for measurements of both solid and liquid materials across a wide range of temperatures.
    - Disadvantage: A major concern for this method is the criticality in ensuring uniform mating/contact with the MUT – particularly when the MUT is a solid. Any slight misalignment or deviation of the probe from perfectly normal to the surface of the MUT will result in inaccurate readings. Conversely, the MUT must have a uniformly flat surface, be homogenous throughout (i.e.: low porosity, no air gaps, cracks, low surface roughness, or other discontinuities), and be of sufficient size; both in area to protrude beyond the footprint of the probe, and in thickness to the extent which no variation in the readings is observed when different materials are present/absent behind the MUT, opposite the position of

the probe. (In instances where the MUT is not sufficiently thick enough for this variation to be eliminated, either the MUT must be suspended such that open air is behind the MUT at the point-of-contact with the probe, or the probe must be suspended above the surface that the MUT will be sitting upon - precisely at the same height as the MUT's thickness - during the 'Open' measurement of the OSL probe calibration procedure).

2. Resonant Cavity: This technique consists of a sealed cavity apparatus in which a sample of the MUT is placed. A test signal injected into the cavity, and the response (reflection and/or transmission) is measured. The system is tuned by varying either the frequency of the test signal, or the size of the cavity. The point at which the cavity resonates directly correlates to the dielectric constant of the MUT present within. This point-of-resonance manifests in the form of a sharp 'dip' in reflection measurements, and/or a prominent peak in transmission.
    - Advantage: This method enables high accuracy and precision of measurements as any/all parasitic characteristics of the two-port cavity itself can be normalized via the 'thru' measurement of a conventional open-short-load-thru [OSLT] calibration procedure.
    - Disadvantage: A major limitation is the maximum sample size the cavity can accommodate. The cavities are themselves limited to a narrow frequency range of operation - particularly those of a fixed size. Achieving

high precision/accuracy in measurements is rather time consuming as attention to detail in both sample MUT preparation and installation/apparatus setup is needed. Any change in cavity size requires repeating the OSLT calibration procedure.

3. Free-Space: This Technique consists of placing the MUT in an open-air signal path between two directional antennas (of known/normalizable characteristics) facing each other at a set distance. The MUT is thus in a 'free space' environment. Like the resonant cavity technique, a test signal is injected into one of the antennas and reflection and transmission characteristics are measured. Any/all deviation from the transmission/reflection response of the open-air system without the MUT in place (the normalized baseline loop transmission), is directly influenced by the MUT's dielectric co

Other methods of dielectric characterization are referred to as "two-port" measurement techniques (in terms of derived S-parameters). These method variants all essentially amount to placing the material in series with a balanced signal path, which, without the sample in place, has been normalized via the 'thru' conventional open-short-load-thru [OSLT] calibration (the thru measurement includes the two-port jig in which the MUT is to be installed). Be it a waveguide, resonant cavity, or even in free space.

For the waveguide method, the sample MUT of sufficient cross-sectional dimensions is placed inside a waveguide in which it completely fills a section of the guide. The resonant cavity method is very similar to that of the waveguide method; however, the sample is of an arbitrary (but known) size that is smaller than the inner dimensions of the cavity walls. Unlike the waveguide method, the cavity's construction (as the method name suggests) is tuned to resonate at a specific frequency with no material inside. In this manner, the insertion of a material will detune the resonator, the extent of which is determined by the materials ε_r and TanD characteristics.

The free space method more-or-less combines parts of the previous two methods. Rather than inserting the MUT in a directly coupled transmission path like the waveguide method, the MUT is instead placed between two directional antennas (of known characteristics) facing each other at a set distance. This method allows for the material to be thin and of more arbitrary shape (not perfectly flat) but must still be rather homogeneous. This method is best performed in a shielded, low noise/reflection environment.

All of these methods were developed ubiquitously under the assumption that only the MUT be present for the measurements. This in turn means that there cannot be any other material, particularly those of the conductive variety, be present, as this additional material will predictably dominate the overall characteristics of the sample and greatly skew the readings. This may appear as a rather trivial point to highlight, but in those rare instances where a 'standalone' sample of the substrate

material is impossible to obtain, this requirement becomes far less than trivial to work around. Such is the case when attempting to characterize the HBN substrate, as it exists post-pyrolization when sandwiched between layers carbon-loaded ceramic.

CHAPTER III

MATERIAL CHARACTERIZATION AND PROTOTYPING

3.1 Background

Hexagonal Boron Nitride was chosen as the base material for this endeavor. It conforms to all necessary fabrication process flow requirements; its originating non-Newtonian liquid state is optimal for the pressure-fed 3D printing apparatus, cures to a machinable solid, and once pyrolyzed, it becomes ceramic-like with rigid thermal stability for up to 900°C (Figure 3.1). By itself, hBN is electrically non-conductive, however, by adding a Carbon filler to the pre-pyrolyzed liquid slurry, the material becomes sufficiently conductive while retaining identical thermal stability properties as that of the standalone pyrolyzed hBN substrate.

In essence, these two variants are functionally identical with respect to their thermal and structural nature, enabling them to be 3D printed cohesively via a dual-nozzle process (Figure 3.2). The two materials ultimately become one contiguous ceramic structure following pyrolyzation, wherein the conductive and non-conductive regions as arranged in the printing process are preserved. As such, a homogeneous workable metal-on-substrate medium is obtained, to which microstrip antenna design and theory may be applied.

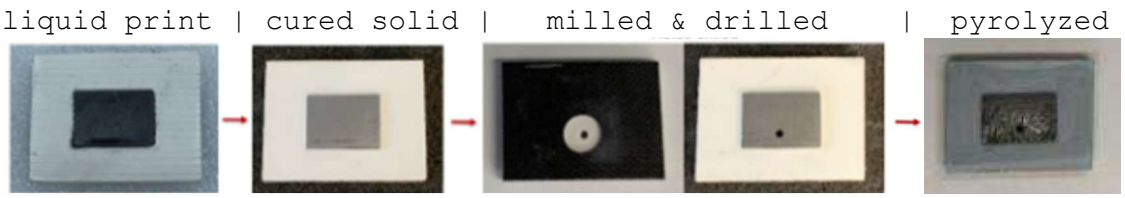


Figure 3.1: Fabrication Process Flow

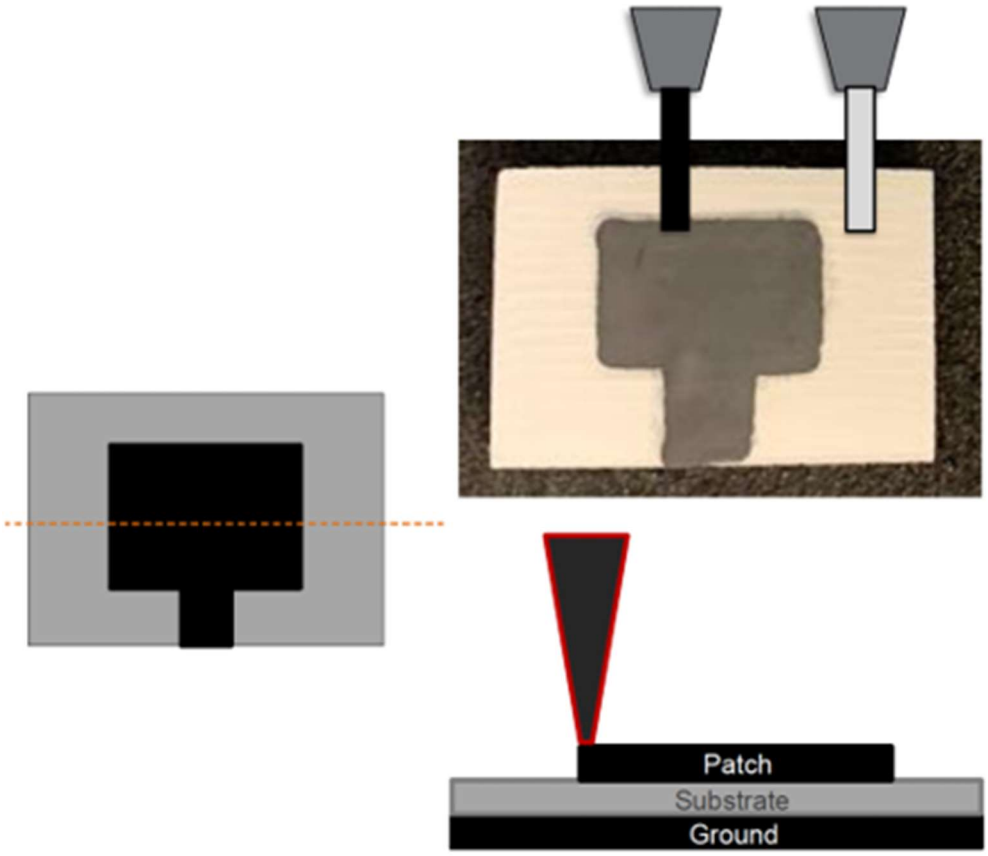
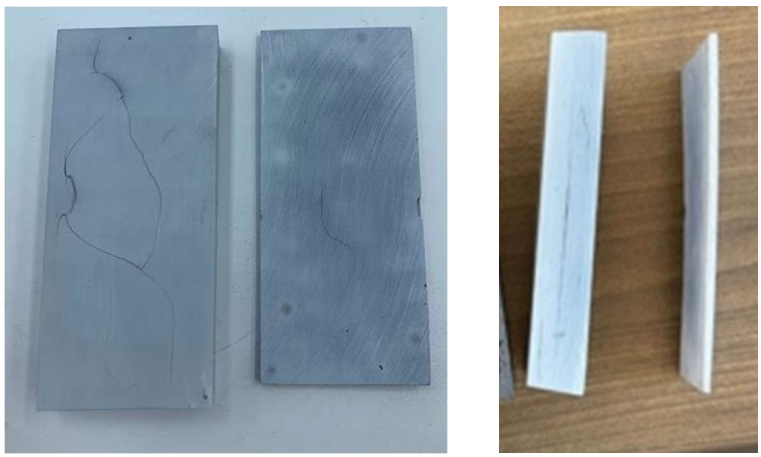


Figure 3.2: Dual-Nozzle Pressure-fed 3D Printing Process

3.2 hBN Preliminary Samples

Sample blocks of varying thicknesses of standalone hBN were obtained for characterization (Figure 3.3a and b). Upon qualitative inspection, some inconsistencies were plainly observed of this early batch, however, these anomalies were somewhat expected and mostly unavoidable given the deliberately exaggerated printing dimensions needed for the characterization process; both an exceedingly thick, and conversely thin sample is needed in order to determine the functional skin-depth of the material. Both sizes of samples exhibited hairline fractures throughout, an occurrence during the pyrolization process. The thin-variant samples were found to have warped to varying amounts during this process as well. Differing levels of porosity throughout the samples were also observed.

Ideally, the substrate must be as homogeneous as possible in order to establish a foundational baseline environment, onto which microstrip structures may be designed. While these early samples were decisively not homogeneous throughout, the inconsistencies were sufficiently spaced apart to where moderately-uniform areas within each sample may be discretely measured using an HP 85070B coaxial dielectric probe (Figure 3.4).



a b

Figure 3.3: hBN Samples of differing thicknesses



Figure 3.4: Hp 85070B Dielectric probe (right) and calibration shorting Block (Left)

3.3 Open-ended Coaxial Probe Measurements

Given the need to take discrete measurements at a variety of different locations across each sample, as well as the need to characterize samples of various geometries, the optimal apparatus for the task is that of the coaxial dielectric probe. This device is, in effect, an open-ended piece of metrology-grade coaxial cable that features a wide-flanged outer conductor and a high-precision 90° cut. The geometry and characteristic impedance (Z_0) of this probe is known. Any/all material directly contacting the end of this probe may be considered a terminating load (Z_L), wherein a reflection coefficient will be present and observable. From this single port scattering parameter (S11), the dielectric properties of the material under test (MUT) may be derived.

Calibration is achieved via a modified variant of the traditional Open-Sort-Load (OSL) method:

- Open: Holding the probe in mid-air.
- Short: Using the gold-plated pressure plate within the provided shorting block
- Load: Immersing the probe in a container of room-temperature water

With these three measurements, 3-term error correction may be performed[2].

Special care must be taken when performing measurements. The probe must remain perfectly flat against the sample (in the case of solid MUTs). Conversely, the MUT must have an adequately

flat planar face with minimal surface roughness and inconsistencies. The MUT should also be of sufficient thickness to the extent that it surpasses the skin depth boundary in order to avoid effects of any/all material present immediately behind the MUT/opposite the probe. To verify that the MUT's thickness extends beyond the skin depth boundary, measurements are taken both with and without the presence of a metallic backing. No change should be observed between these two conditions if the boundary requirement has been met/surpassed. This verification was performed for all sizes of samples.

A suitable preliminary approximation of the dielectric constant (ε') and loss tangent (ε") was obtained by averaging together numerous measurements of different areas across all samples (Figures 3.5 and 3.6). Among all samples measured, the net-average dielectric appeared to hover at around 4.6.

3.4 Transmission Line Measurements

With a rough preliminary dielectric constant of 4.6 obtained, one of the more uniform/homogeneous thin samples was selected for an additional test. Copper tape was applied covering both faces of the sample. On one of the faces, the tape was then carefully carved out to create a transmission line (Figure 3.7a). The width of the transmission line was determined with the aid of PCAAD (Figure 3.7b).

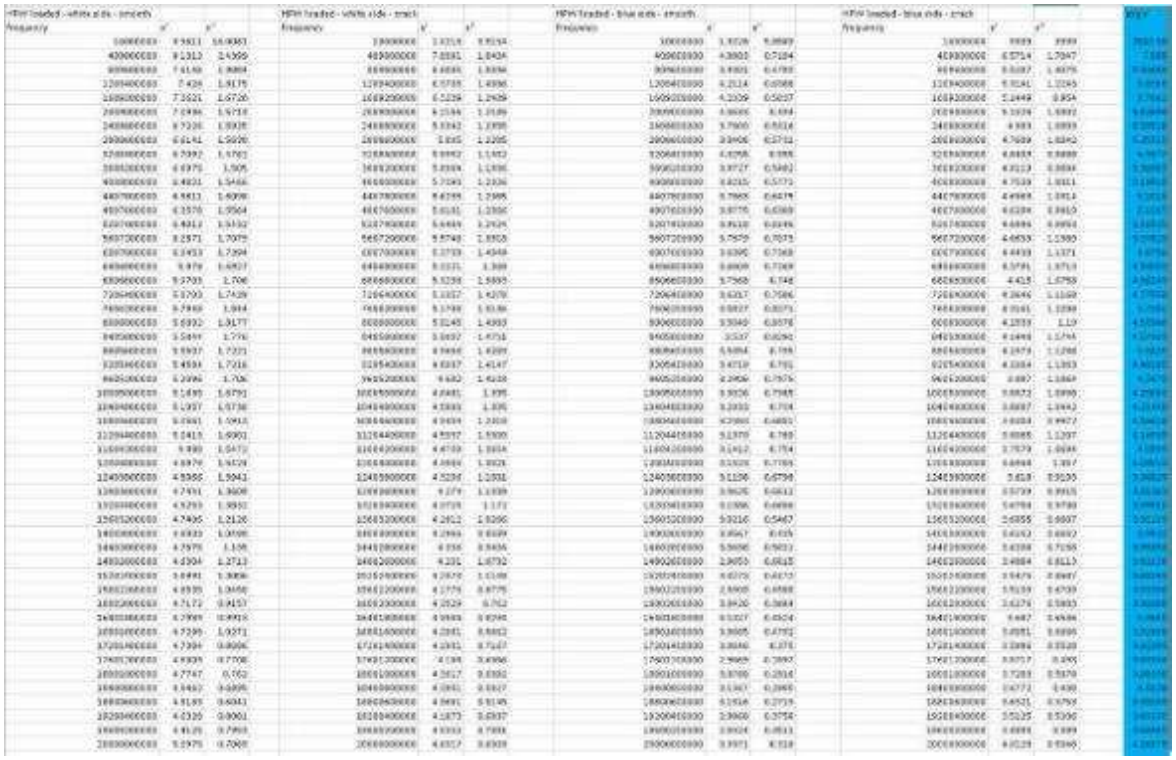


Figure 3.5: e’ and e” measurements taken across each of the preliminary samples

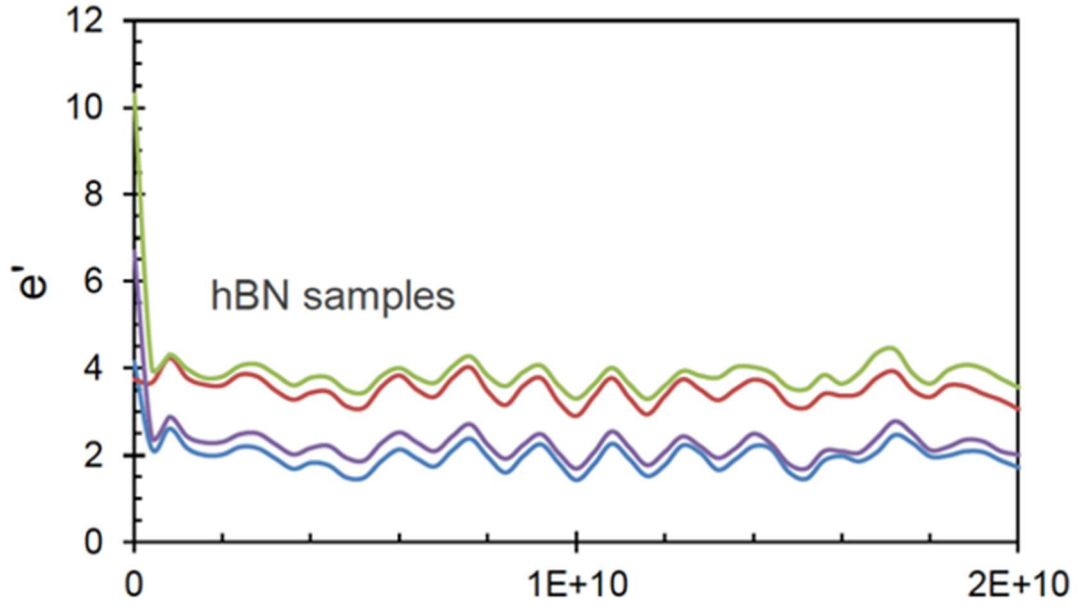
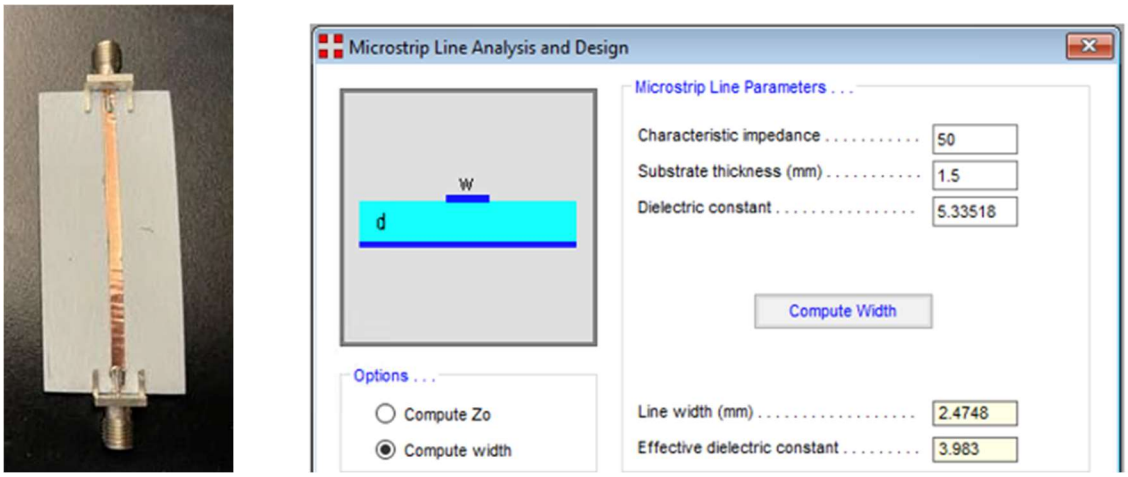


Figure 3.6: Average dielectric constant vs frequency measured for each preliminary sample



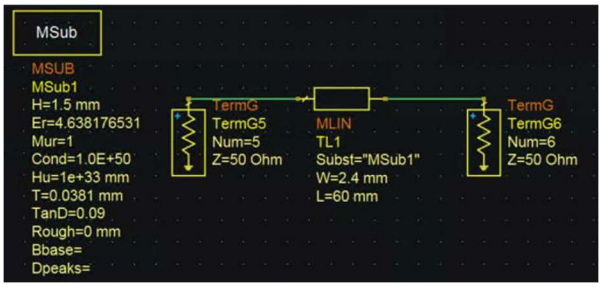
a b

Figure 3.7: Copper transmission line on selected thin preliminary hBN substrate sample (a) with line width as determined using PCAAD (b)

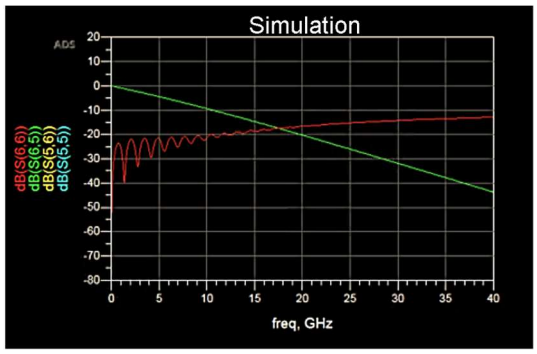
An S-Parameter sweep of the transmission line was performed. The resultant reflection and transmission coefficients were transferred into Keysight/PathWave Advanced Design System (ADS) in order to compare them against a simulated design of the transmission line and substrate. This sim model had also been designed based on the preliminary findings from the dielectric probe measurements (Figure 3.8). As expected, some minor discrepancies were observed between the simulated transmission line and the handmade copper line prototype. Tuning of the E_r and TanD fields brought forth a sim model with a similar (albeit, broad) complement of response curves as those of the experimental results.

3.5 Resonant patch antenna design

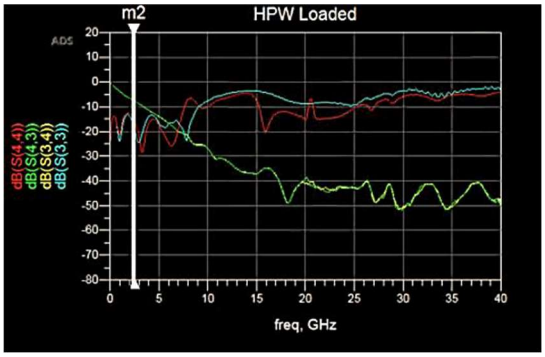
Although 3D printing enables an increasingly wide range of intricate shape and structural creation, a simplistic patch antenna topology was determined to be the optimal design "Benchy" (a term used in the 3D printing industry for a standardized benchmark test structure) for this inaugural voyage into exploring the application potential of this novel medium. Such a baseline structure allows for close examination and optimization of all aspects of material, design, and fabrication precision and flexibility as it relates specifically to RF applications, while simultaneously highlighting the dual-nozzle/dual-material capabilities specifically lucrative to space-based technologies.



a



b



c

Figure 3.8: ADS Sim model of copper transmission line (a) and S-parameter response curves of both the ADS sim model (b) and the copper transmission line (c)

Considering the equipment available for fabricating these prototype structures, the volumetric real estate available in which these antennas may be designed was, in effect, heavily limited. A target frequency of 10GHz was selected as a compromise between manufacturable space and minimal precision demands. A lateral-fed patch antenna was designed initially using PCAAD, then simulated in CST. The CST simulation predicted moderately sufficient performance with a gain of 3.85dBi at the target frequency (Figure 3.9).

Upon receiving the inaugural bath of antennas, the first major hurdle emerged in the form of coupling the antenna to conventional hardware. An earlier analysis of the carbon samples revealed that the material would not accept traditional solder. The original planned workaround was to apply a copper tape pad to the feedline and ground plane thus to provide a solderable surface to which a standard SMA edge connector could be installed (Figure 3.10).

It quickly became evident that the tape's adhesive is inadequate for the carbon surfaces, leading to an unreliable connection to the antenna, both mechanically and electrically. A conductive silver-based epoxy was identified as a viable solder substitute (Figure 3.11) that can reliably adhere to both the carbon surface as well as the plated conductors of the SMA connectors.

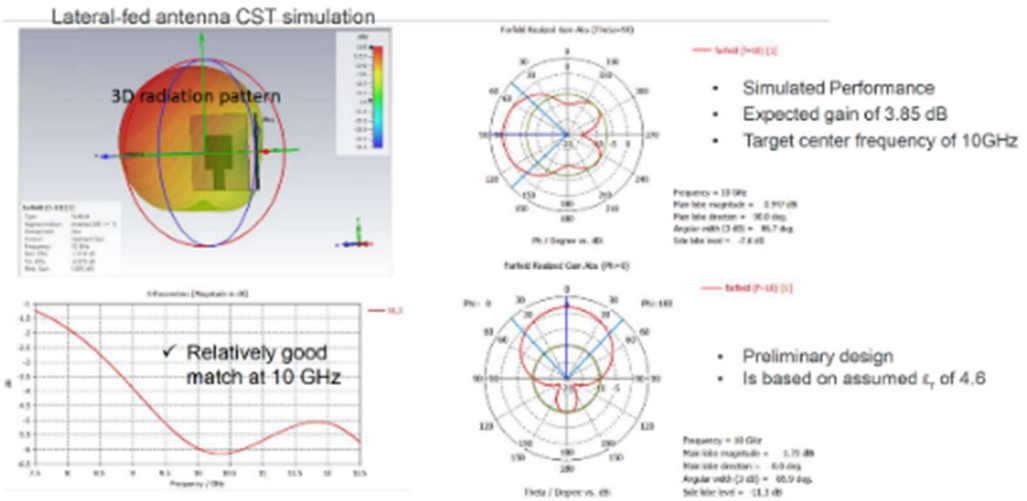
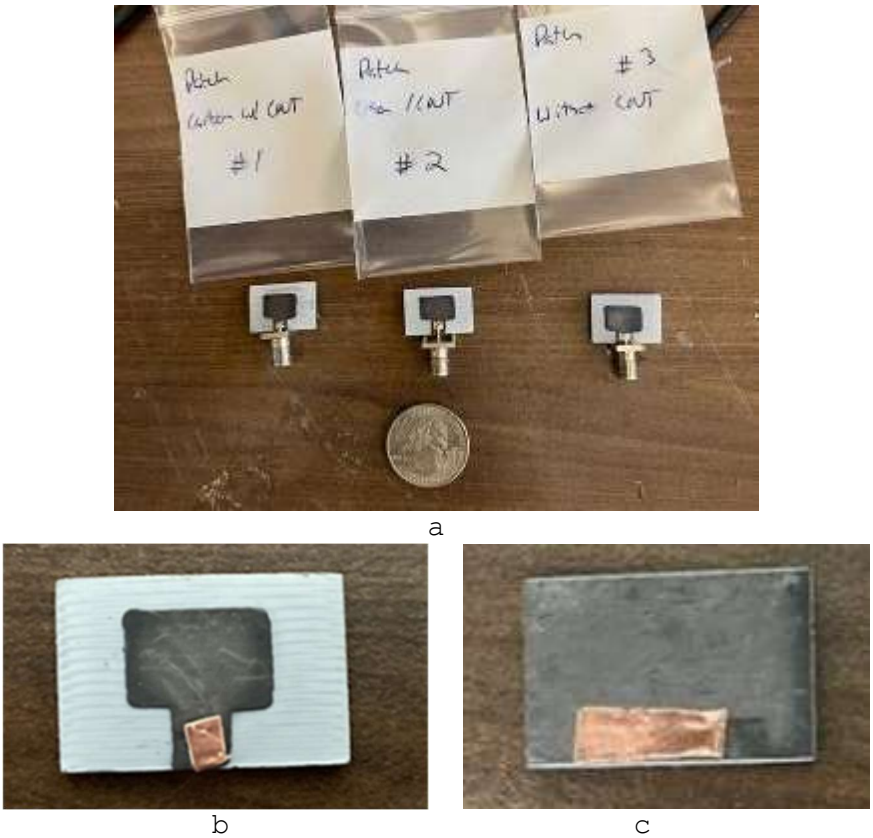


Figure 3.9: CST design of lateral-fed patch antenna



a

b c

Figure 3.10: First batch of antennas (a) with initial attempt of coupling to SMA connector via copper tape pads on both the feedline (b) and ground plane (c)



Figure 3.11: Improved coupling achieved via silver epoxy

Measurements of this inaugural batch revealed a sharp deviation from the performance metrics predicted by the CST simulation; far exceeding any anticipated, acceptable marginal discrepancies typical of the contrast between simulations and practical implementations. The resulting resonant frequency of the antennas had effectively been reduced by approximately 50% of the targeted 10GHz (Figure 3.12). Caliper measurements of the patch elements immediately ruled out a deviation in physical dimensions as a potential culprit. A copper tape/FR4 equivalent antenna additionally confirmed this (Figure 3.13). This substitute antenna did, however, highlight the feedline as being a potential bottleneck.

Considering both the criticality that impedance matching has on the overall performance of an antenna, and with confirmation that the silver epoxy is a suitable coupling material between the antennas and conventional hardware (thus eliminating the necessity for specifically an edge connector), a decision was made to abandon the lateral feedline approach, opting instead for a coaxial fed patch design (Figure 3.14). The hypothesis in this move was that it might two-fold isolate and eliminate the potential impedance mismatch resulting from the feedline, and to minimize the loss as observed across the entire range of the reflection measurements. With these modifications made, should a similar sharp deviation be observed in the second batch as

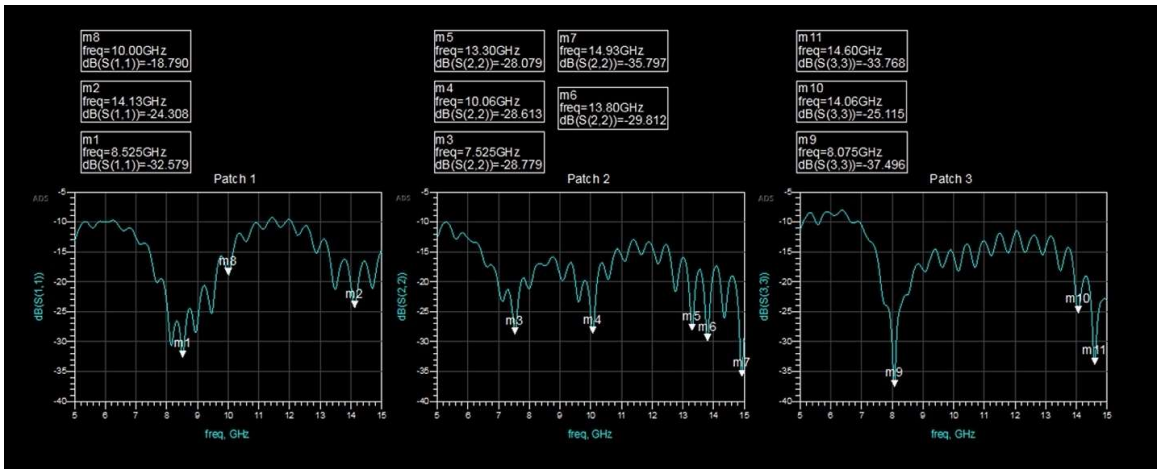
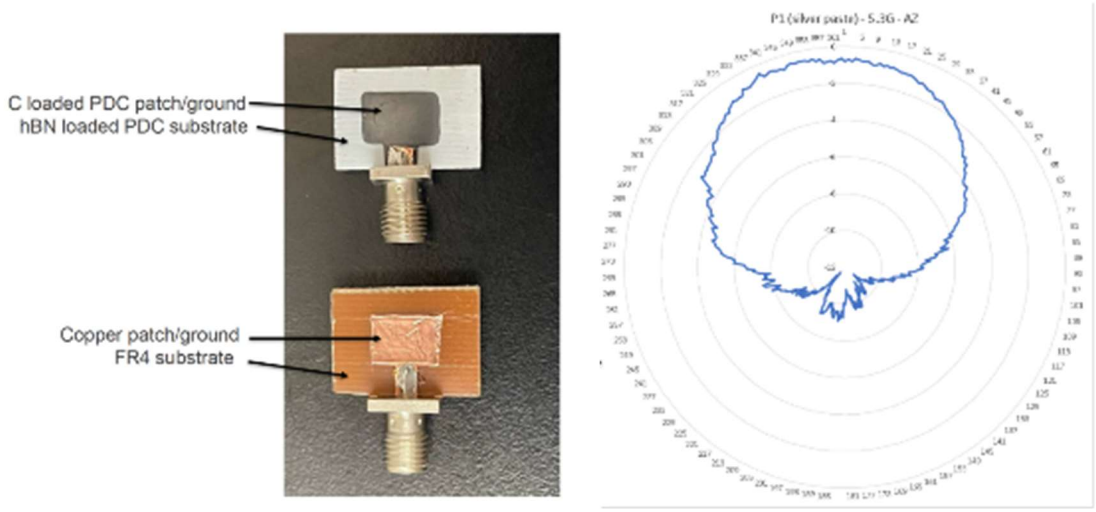
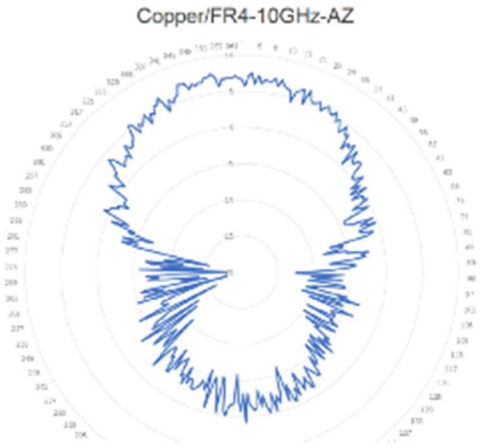


Figure 3.12: Reflection measurements of first antenna batch

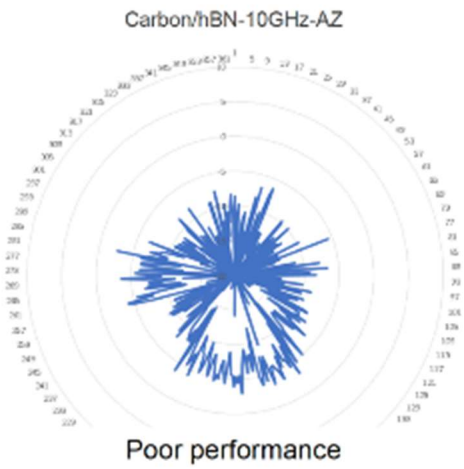


a b

Figure 3.13: Ceramic Batch-1 antenna compared to copper/FR-4 reference antenna (a), maximum gain of ceramic antenna at ~half the target frequency (b), confirmation of expected performance at 10GHz using copper reference antenna (c) compared to performance of ceramic antenna at 10GHz (d)



c



d

Figure 3.13 continued

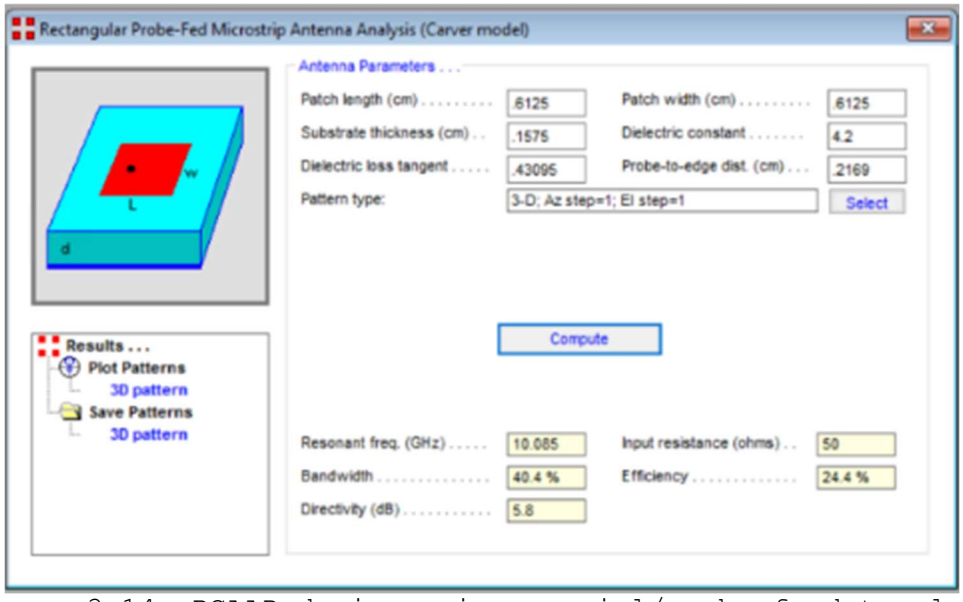


Figure 3.14: PCAAD design using coaxial/probe feed topology (specifically of copper/FR-4 reference design also fabricated)

observed in the first, the substrate's dielectric properties would be called back into scrutiny.

During the fabrication of the second batch, clues began to emerge as to the underlying cause of the discrepancies. Following installation of the SMA ports on the antennas, a continuity check was made to verify that the silver epoxy hadn't seeped through and inadvertently shorted the patch to the ground plane. All antennas were found to have conductivity between top and bottom layers, including those which had not yet had an SMA port installed. Subsequent material testing determined that the carbon in the patch and ground elements would migrate into the substrate layers during pyrolysis; drastically shifting the dielectric constant and loss tangent of the now-encapsulated substrate to an unknown quantity. (Figure 3.15)

Reflection and transmission measurements performed on this second batch (Figure 3.16), while retaining a drastically lower resonant frequency much like those of the first batch, showed significantly improved gain and directivity (Figure 3.17). To investigate the potential underlying shift in substrate properties and, moreover, to validate the theory that the substrate's dielectric constant had indeed changed as a result of carbon migration during pyrolysis, a series of reflection measurements were taken while iteratively de-tuning the antennas

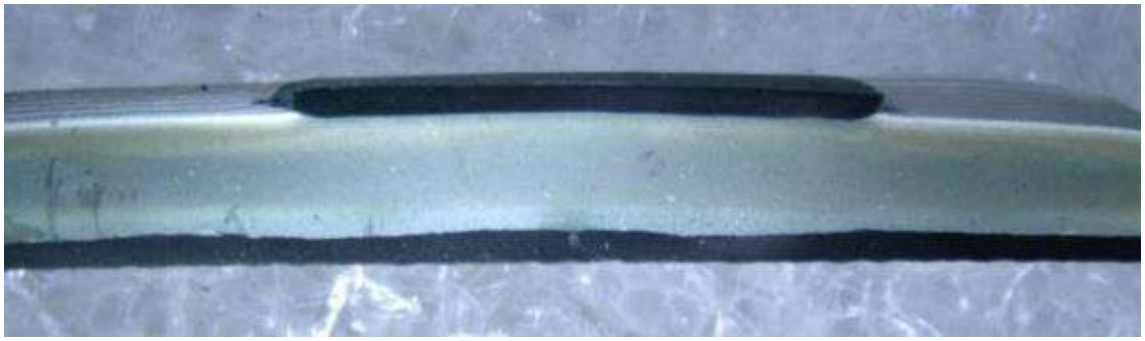


Figure 3.15: Macro/cross-sectional view of patch antenna. Dark-shaded discoloration is carbon that has migrated into the substrate

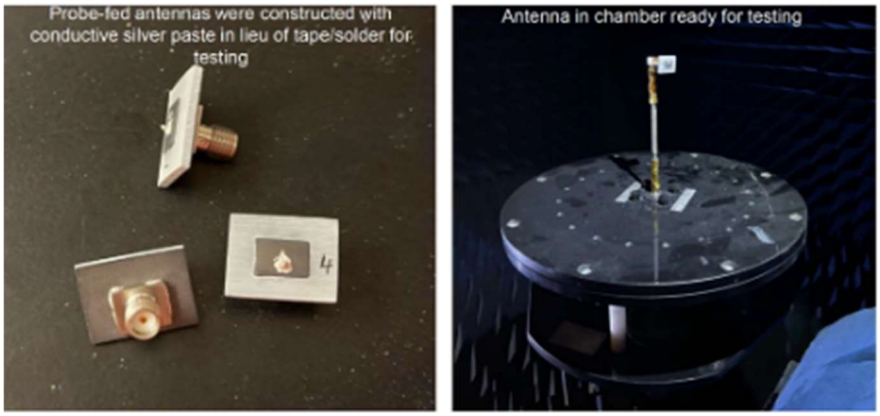
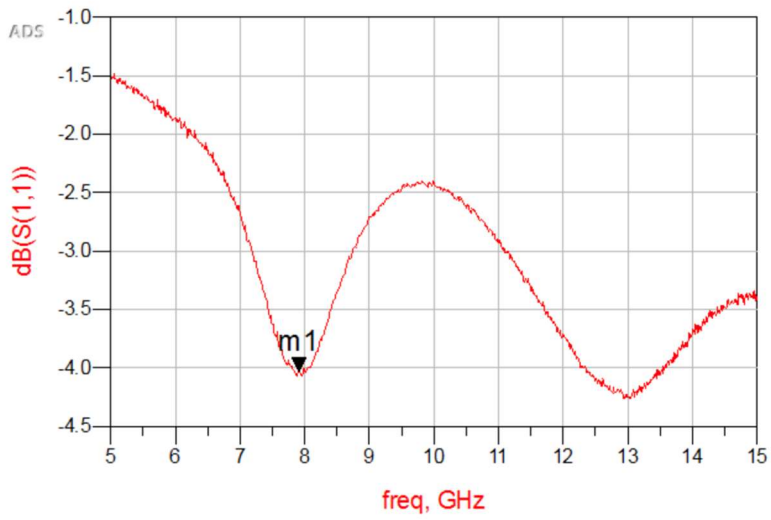
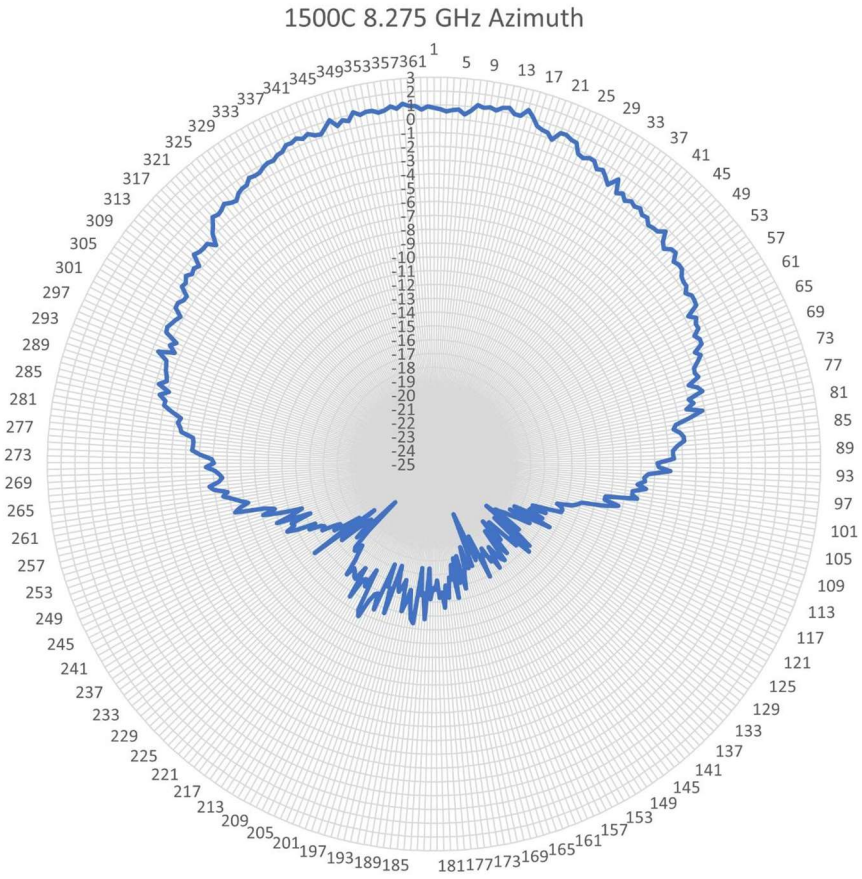


Figure 3.16: Batch-2 antennas



a



b

Figure 3.17: Batch-2 antenna with lower-than-expected resonance frequency (a), but much improved gain performance (b)

by adding specified lengths of copper tape to the patches (Figure 3.18).

The measurements were imported into CST alongside sim models created for each net-patch size case. A parameter sweep was performed on the sim models iterating the ε_r value until the simulated reflection response matched those of the measured results (Figure 3.19). The sim responses converged to align closely with the measurement plots; the dielectric constant had indeed changed (Figure 3.20).

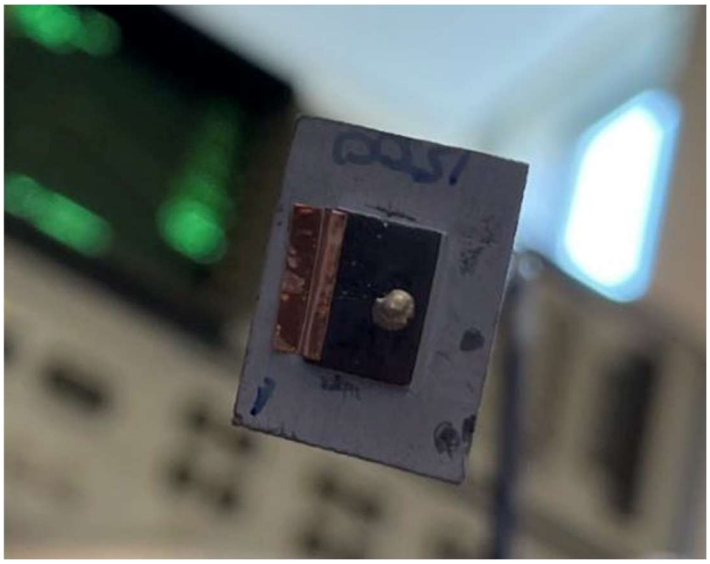


Figure 3.18: Copper tape added to antenna to lower resonant frequency

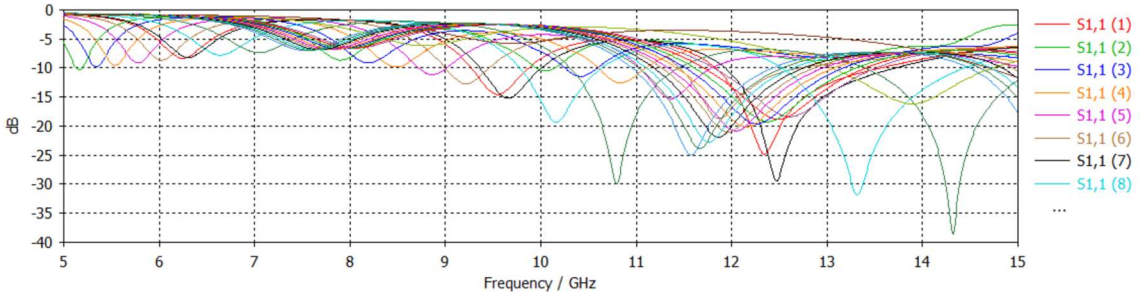


Figure 3.19: CST E_r parameter sweep

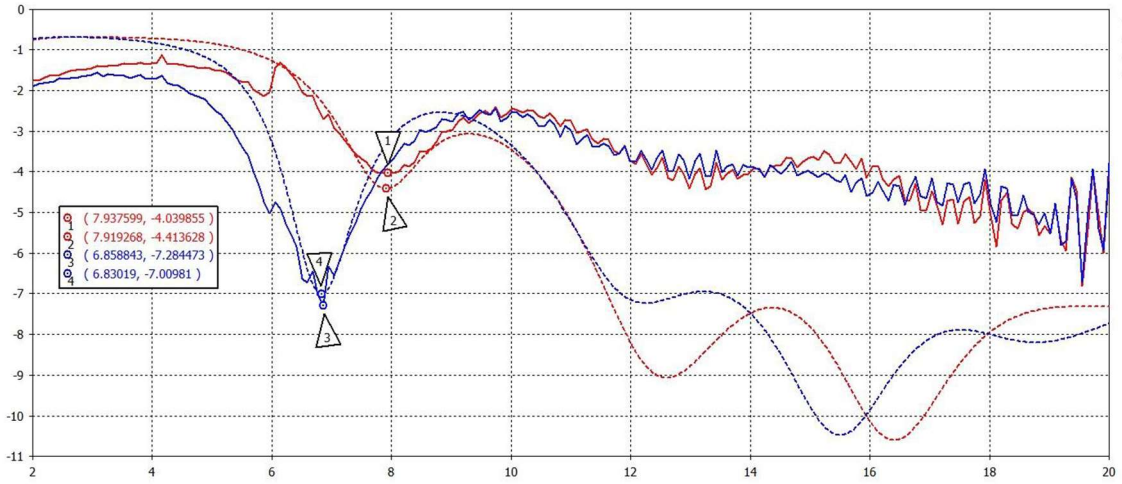


Figure 3.20: Reflection measurements of antenna (solid traces) before (red) and after (blue) adding copper tape. With the E_r simulation parameter set to 5.8, the simulated reflections (dashed traces) track that of the measured results

CHAPTER IV

HIGH TEMPERATURE ANTENNA TESTING

4.1 Background

Given the overall promising outlook regarding the ability to 3D print preceramic polymers into functional antennas, the final facet yet to be tested is the antenna's robustness to extreme temperature swings. The leading face of any vessel traveling at hypersonic speeds through a fluid medium will undoubtedly experience temperatures in excess of 1000°C. Airframes designed to withstand these temperatures often have an ablative exterior surface, intended to burn away as a sacrificial material in order to protect the cargo within. In instances where reusability is desired, film cooling is the preferred method.

Since the objective for these antennas to remain intact and functional following a hypersonic excursion, these antennas would certainly not be incorporated as part of the sacrificial layer, rather, either be protected by this layer, or installed on a non-prevailing face of the vessel. While the antennas will be spared of the highest temperatures in this configuration, the localized temperatures it may still experience would be well into the hundreds of degrees Celsius. It was determined to conduct tests up to 900°C.

4.2 High Temperature Testing - Logistical Considerations

To conduct tests at these temperatures in a laboratory/controlled environment setting, special equipment is needed. Most critically needed is a feed line and connection that can subsequently survive these test temperatures. Custom coaxial lines fabricated by T-Axel were acquired (Figure 4.1) for this purpose. These rigid 50Ω lines are rated up to 1000°C operating temperature and 18GHz operating frequency. The lines were custom designed to be 15 inches long with a 90° bend towards the open 'hot' end to which the AUT would be installed (Figure 4.2). The other end was fabricated with a female SMA connector built-in, facilitating connection to the network analyzer via standard APC-3.5mm test port cabling. The AUT is connected to this line in an identical manner as that of the previous tests using SMA connectors, now with a solder substitute bonding material in the form of Pyro-Duct 597 Silver epoxy, rated to 927°C (Figure 4.3).

The conventional SMA connectors used in previous measurements featured an outer conductor inside-diameter of 3.5mm. Prior to pyrolization, the ground planes of each antenna had already been drilled out by this diameter down to the substrate layer, surrounding the inner conductor's drill hole that extends through the entire antenna. The SMA connectors also featured a sufficiently wide flange extending outwards laterally from the opening, allowing for a robustly stable physical connection and alignment.



Figure 4.1: High temperature coaxial feed line



Figure 4.2: Open 'hot' end of high temperature line. Dielectric filler appears to be aerogel. (T-Axel would not disclose any information regarding specific materials or construction methodology, deeming it a trade secret.)



Figure 4.3: Aremco High Temperature Conductive Silver Epoxy

The high temperature feed lines lack this flange, and the outer diameter of the hot end is smaller at approximately 2.4mm. Full insertion of the line into the antenna results in both its outer conductor and dielectric filler resting against the antenna's substrate layer, having sunken through the opening in the ground plane. To both electrically and mechanically accommodate this, silver epoxy is simply packed into the resultant 550µm-wide crevice between the outer perimeter of the feed line and the inner wall of the ground plane (Figure 4.4).

While an immediate (albeit, modest) benefit of this is the absence of an air gap between the line's dielectric and the substrate – an additional discontinuity that normally results in a minor, yet functionally negligible amount of impedance mismatch and loss – the difficulty in physically mounting the angled line to the antenna is greatly compounded, as the silver epoxy requires a 4-hour cure time: 2 hours at room temperature, followed by 2 hours at 97°C. A jig, using readily-available materials capable of these curing temperatures, was fashioned together using sheet aluminum, a silicone mold, and copper tape facilitated the joining of antenna and feed line (Figure 4.5).

A variant of the high temperature line was also fabricated to feature a female SMA connector on both ends (Figure 4.6). During the initial OSLT calibration procedure, this line is installed in place of one of the antenna-mounted lines, enabling a port extension line of approximately identical properties to be

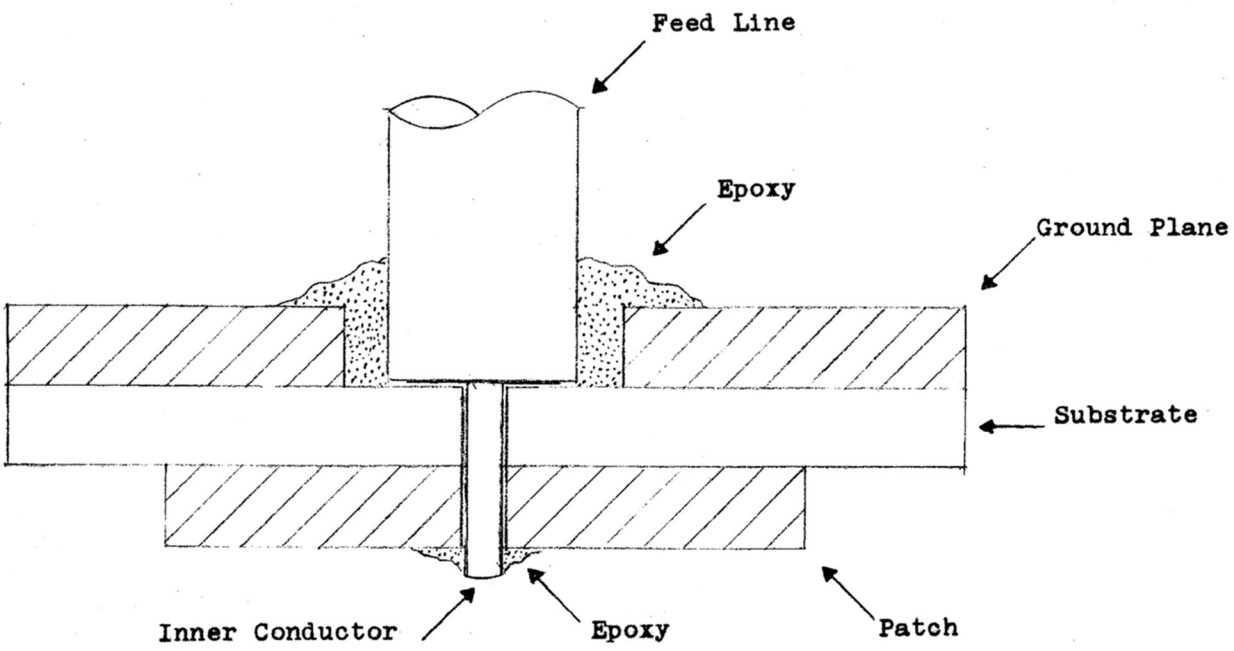


Figure 4.4: Cross section of antenna and feed line connection



Figure 4.5: Antenna-to-feed line mounting process using jig



Figure 4.6: High temperature reference/thru line featuring an SMA connector on both ends

included in the calibration (Figure 4.7), thus the calibration plane may be relocated to the contact points on the antenna itself, as was the location for all prior room temperature measurements.

Several methods with which to apply heat to the antennas during the tests were evaluated, each presents their own sets of advantages and disadvantages. The primary criterion of these tests requires that the heat source device itself not intrude upon and/or interfere with the RF signal environment of the test apparatus. In effect, the heating device must be physically absent from the measurement plane. For this reason, heating via direct contact with the AUT is not an option, as the device will impose an unaccountable shift in the AUT's reflection characteristics.

For transmission/radiation measurements, an additional constraint emerges requiring not-only that the heating device not be in the direct line-of-sight path between the AUT and reference antenna, but that its proximity and orientation be sufficiently removed and positioned such to prevent incidental absorption and/or multipath-reflections of the radiated signals. As such, the heating device may be positioned neither broadside, nor behind the AUT during the tests.

Another critical facet to be considered in heat source selection pertains to both the speed and precision of its ability to control the AUT's temperature for the duration of each test.



a

Figure 4.7: Reference line connected to VNA (a) and S21 measurement of the line (b)



b

Figure 4.7 continued

Given the intended hypersonic applications of these antennas, rapid plasma-derived heating of the AUT would pose the most faithful emulation of such an environment. However, regarding the overarching practicality of available equipment, an inverse relationship exists between the rate of the AUT's temperature swing, and the effective precision of both discretized temperature control and RF measurement sampling.

It was determined that two categories of tests be performed, using differing modes of heat application/temperature control, to be the optimal choice under the given circumstances:

- Reflection-only tests: These are performed with the AUT inserted into a kiln furnace, wherein the temperature is ramped up and down in a slow, controlled manner ('Furnace Tests').
- Reflection/Transmission tests: These are performed in open-air wherein the AUT is pointed towards a reference antenna positioned 1 meter away. Heat is applied rapidly to the AUT's face via a tangentially positioned MAPP gas torch ('Torch Tests').

4.3 Furnace tests

This test format allows for a very high degree of discretized controllability of the ambient temperature encompassing the AUT, however, the maximum rate of temperature

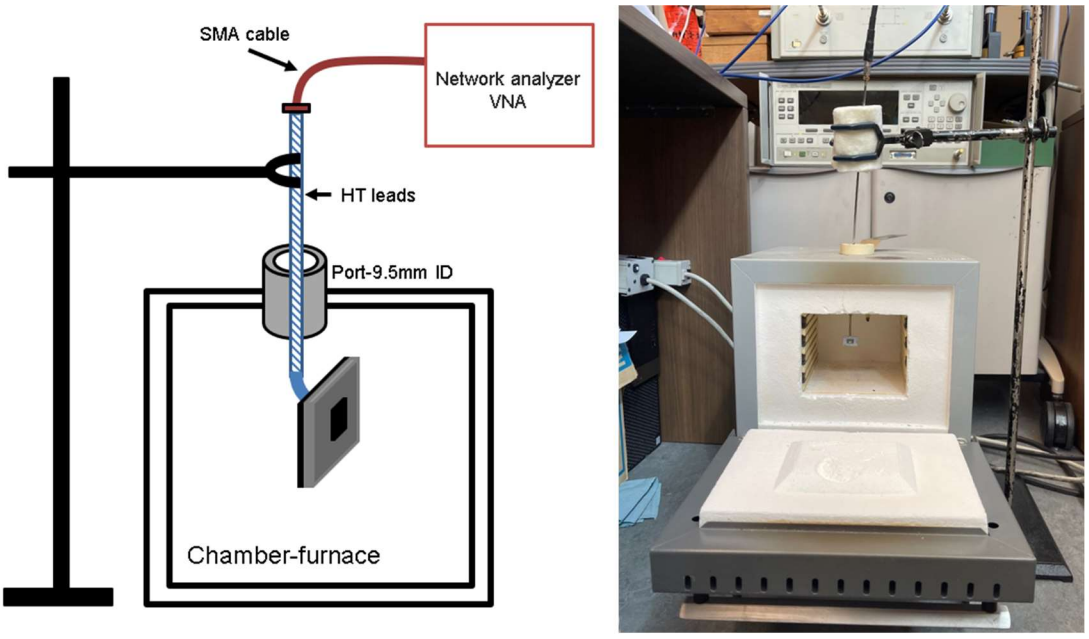
swing is greatly reduced. The ability to measure the AUT's radiation performance is also sacrificed outright as the furnace completely encapsulates the antenna on all sides, save for the 9.5mm exhaust orifice though which the AUT and feedline is inserted. Additionally, the reference horn is decisively incapable of withstanding the temperatures that the the furnace will reach, thus conducting tests with both antennas in the furnace is not an option.

The Apparatus consists of a Barnstead Thermolyne 47900 Furnace capable of reaching 1000°C (Figure 4.8). A retort stand is positioned directly over it featuring an insulated clamp. An AUT, bonded to the end of a high temperature line, is lowered into the furnace (initially at room temperature) through the furnace's topside exhaust port. The protruding SMA-end of the high temperature line is clamped to the retort stand, positioned such that the AUT is freely hanging in the volumetric-center of the furnace cavity. (Figure 4.9)

An initial test was performed ramping the temperature up to the halfway point of 500°C. This allowed for testing of all components in the system to a point below the hypothesized threshold in which the carbon in the conductive layers begins to oxidize. Beginning at 100°C, the furnace was increased in 50° increments until 500°C was reached. For each 50° advancement, the furnace was held at the temperature for 10 minutes prior to performing an S11 measurement to ensure uniform temperature



Figure 4.8: Barnstead Thermolyne 47900 Furnace



a b

Figure 4.9: Diagram of furnace test apparatus (a) and actual setup (b)

distribution throughout the cavity. As hoped, the AUT, epoxy, and feedline all survived with minimal deviation in reflection characteristics. (Figure 4.10)

The test was then repeated, this time sweeping across the full 900° temperature range (Figure 4.11). As expected, the prolonged exposure of the carbon layers to ambient oxygen at temperatures above 500°C resulted in oxidation (Figure 4.12), presenting initially as a uniform, exponential increase in loss. When temperatures exceeded 700°C, the carbon immediately surrounding the epoxy bond points with the feedline began to disintegrate. At this point, the resonance was lost, as indicated by a corresponding sudden shift and flattening of the response curve beginning at 800°C. (Figure 4.13)

Given the duration of this test, which was approximately 3 hours and 36 minutes, combined with the fact that this test was performed in ambient air at approximately 886 feet above sea level (this test was performed in Knoxville, TN) wherein the abundance of oxygen is roughly 20% (as compared to 30,000 feet, wherein the abundance drops to 6.1%), the results of this test should be regarded more as that of a "worst-case" test to imminent failure rather than a benchmark of performance of the antenna and/or materials for their intended application of hypersonic robustness. A significant modification to the test apparatus, specifically, a way in which to precisely control the air composition, at any pressure ranging from zero to one atm,

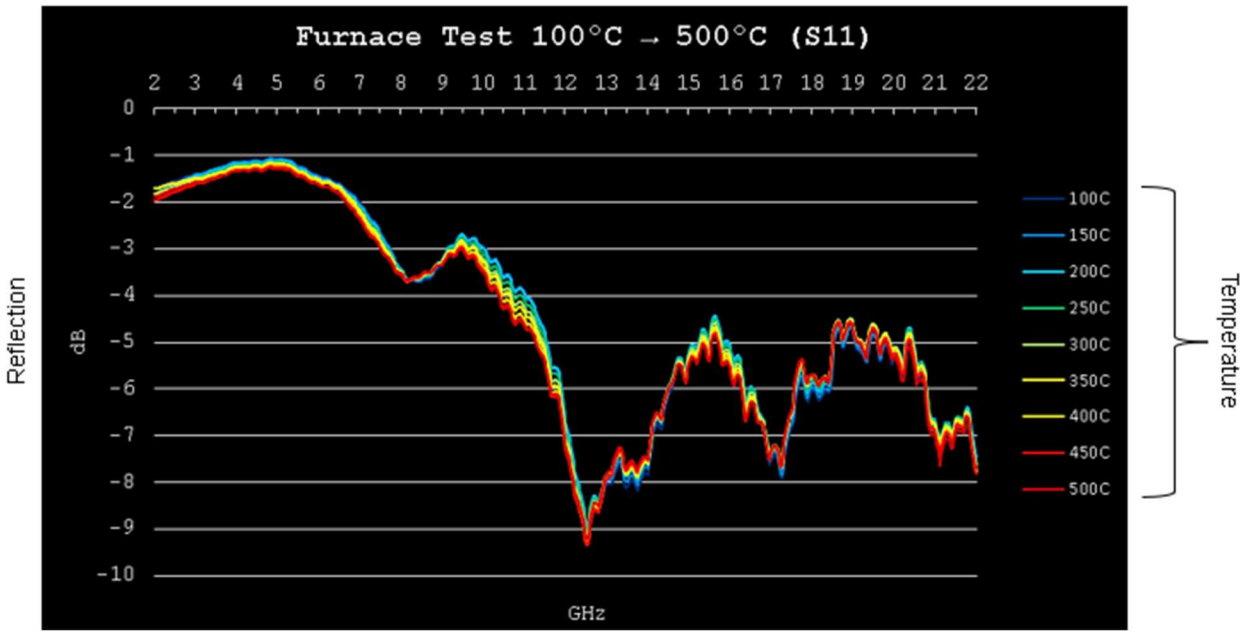


Figure 4.10: S11 measurements of AUT in furnace, temperature swept from 100°C to 500°C. Minimal deviation observed.

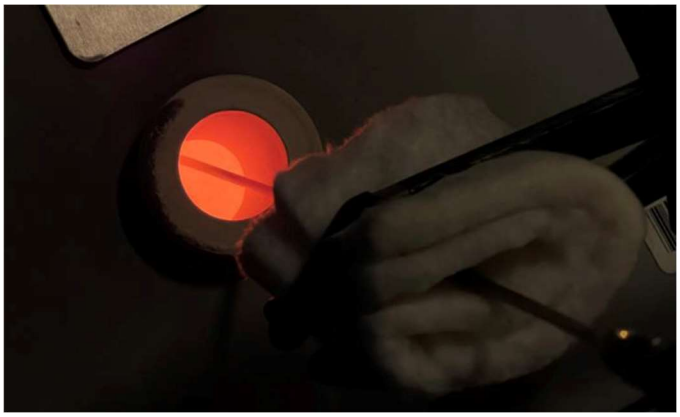


Figure 4.11: Furnace test at 900°C

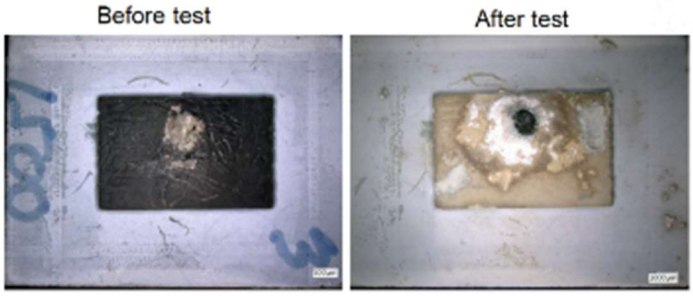
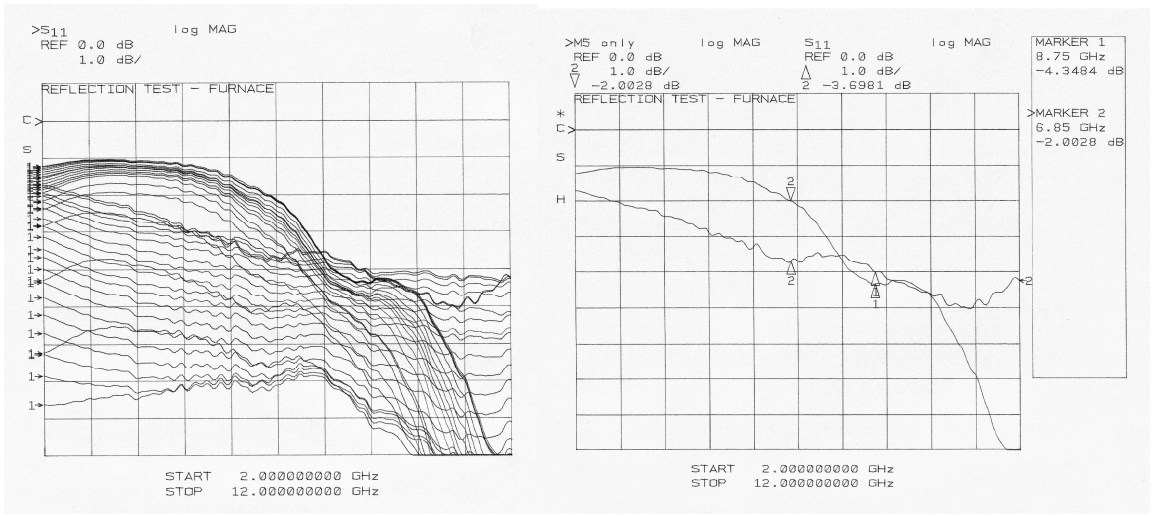
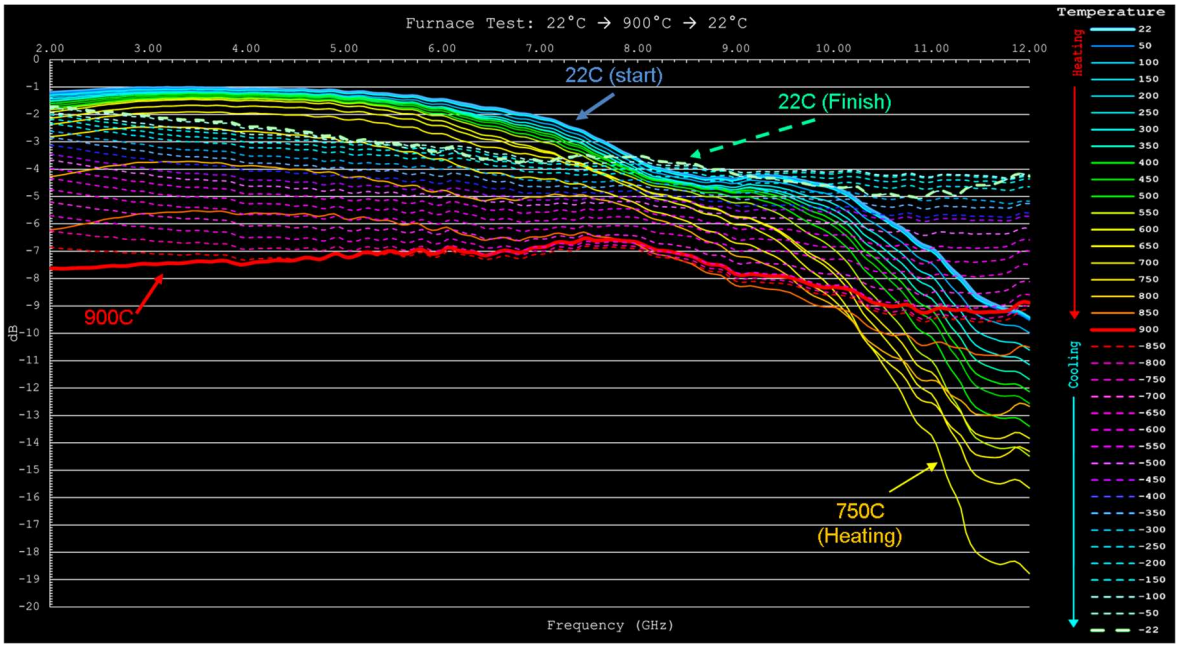


Figure 4.12: Macro view of antennas before and after 900°C Furnace Test Color change in carbon layer indicates oxidation



a b



c

Figure 4.13: S11 measurement results from 900°C Furnace test – plotted response curves from temperature sweep (a), initial and final room temperature measurements compared (b), detailed full temperature sweep (c)

would be required to simulate the tests at altitudes approaching the Kármán line. This would, however, be feasibly impractical.

A supplementary workaround of this challenge is to greatly reduce the duration of the experiment, however, even when eliminating the 10-minute hold at each temperature increment, accounting for only one hour of the duration, the rate at which the furnace itself is able to ramp up and down the temperature is far too slow to sufficiently mitigate the effects of oxygen exposure. A faster method of heating is required.

4.4 Torch Tests

This format circumvents many of the limitations encountered during the furnace tests, while also providing a significantly more faithful simulation of the effects of hypersonic transit. MAPP gas combustion products reach approximately 2925°C on average, nearly triple the target temperature of the test, thus the rate at which the antenna may be heated to 900°C is greatly accelerated, mitigating the duration of the carbon layers' exposure to ambient oxygen while incandescent. The lack of a thermal enclosure also permits measurement of the antenna's farfield radiation characteristics. Some sampling precision, however, is sacrificed.

Network Analyzers, in essence, are comprised of a swept tracking generator, and, at minimum, three spectrum analyzers all operating in tandem. Upon exiting the tracking generator, the

signal is sampled by the first spectrum analyzer channel, designated as the ‘Reference’ (‘R’) channel. The signal continues forward through a directional coupler, and out to the DUT. The second spectrum analyzer channel, designated as the ‘A’ channel, is connected to the reverse-oriented coupled port of the directional coupler. This channel samples any/all signals flowing backwards into the directional coupler from the DUT.

A single-port reflection Scattering parameter, S11, is obtained by dividing the detected returning signal into A channel by the outgoing signal detected by the R channel (A/R). Should the DUT have a second port, it is connected typically through a second directional coupler, to which the third ‘B’ spectrum analyzer channel is coupled in the same manner as the ‘A’ channel. A two-port Transmission Scattering parameter, S21, is obtained by dividing the detected signal at the B channel by the R channel. To obtain the remaining reflection parameter S22 and transmission parameter S12, either the DUT’s port connections are reversed, thus A/R now provides S22 and B/R provides S12, or the connection from the tracking generator is swapped to input of the B channel’s directional coupler [a termination is placed onto whichever coupler is input not connected to the tracking generator], wherein B/R then provides S22 and A/R provides S12.(Figure 4.14) The resulting channel-over-reference ratioed trace data from each measurement configuration is routed into an ADC for quantization, after which the accuracy may be enhanced

further via the 12-term error correction process; the coefficients for which are gathered through the OSLT calibration procedure. (Figure 4.15)

As a result, each S-parameter measurement produces two sets of data (reference and either A or B channel data) that must be processed. Moreover, trace precision within each measurement across the frequency domain is dependent on both the sweep rate and quantized increment for each datapoint. In turn, a higher sweep resolution requires a slower sweep rate, and creates twice-more the data that must be processed; further increasing the overall latency in performing each measurement. Vector network analyzers compound this by further doubling the amount of data due to the retained phase information of each channel. In most scenarios, this inherent latency, ubiquitous of network analyzers, is rarely a critical area of concern. For the torch tests, however, this latency becomes the sole bottleneck for sampling precision in the experiment, as the change in reflection and transmission response curves are significant not only in relation to the AUT's temperature, but in relation to time as well.

With the use of a MAPP gas torch reducing the time for the AUT to reach 900˚C by several orders of magnitude (relative to the furnace tests), a rapid automated control system is necessitated in order to efficiently facilitate acquisition,

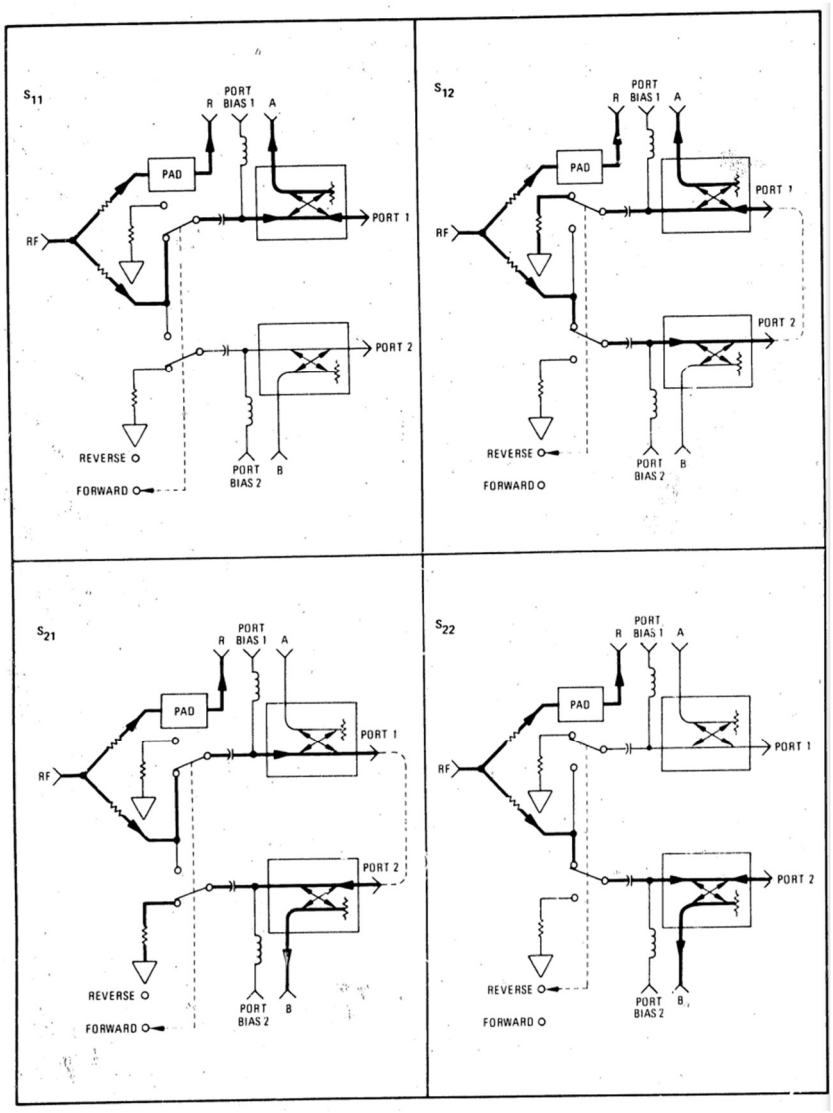


Figure 4.14: Signal flow path for all four Scattering Parameters (HP 8503A Manual)

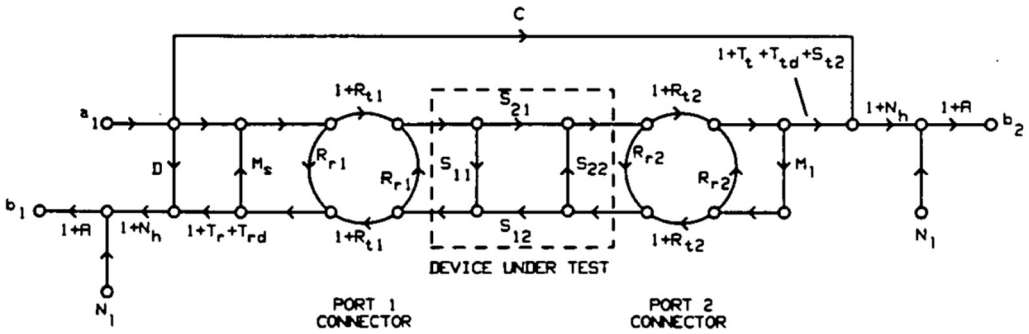


Figure 4.15: System flow diagram for full 12-term error correction (HP 8510B System Manual)

processing, and transfer the large repetitive batches of five-component trace data points (frequency, S11 real & imaginary, and S21 real & imaginary), produced by each reflection and transmission measurement cycle of the network analyzer.

To maximize this cycle rate, the network analyzer must be as streamlined as possible to the extent that it primarily operates off of its hardware alone in performing the fundamental functions detailed above: generating a swept signal, sampling the R, A, and B channels, normalizing the A and B channels against the R channel, and digitizing the results. The 12-term error correction would be the only digital computational process to remain onboard the VNA prior to immediate transfer of the data off the machine for all remaining processing.

An HP 8510B VNA, circa 1992, was determined to be the most optimal for this endeavor as it has the least amount of software interfacing between the ADCs and an external controller, among equipment available for the tests. This system operates natively via the HP Information Bus architecture standard (HP-IB), allowing for direct, parallel, bidirectional signaling link between the 8510 and attached controller.

The controller, an HP 9000/300 computer of the same vintage and architecture, would serve as the intermediary liaison between the 8510 and a modern computer; cyclically running a custom procedural program, written in HP BASIC, that operates as follows:

1. [Start] Initialize system (define variables, establish HP-IB connection to 8510 putting it in REMOTE mode, establish RS-232 Serial connection to modern PC for data export, pre-draw plot fields, zero the “Capture” counter, etc.)
2. Prompt the 8510 to initiate [first] swept measurement of both reflection and transmission parameters
3. Rapidly transfer the resultant, error-corrected trace datasets, off the 8510 onto the 9000/300
4. Prompt the 8510 to initiate the next measurement sweep*
    * The remining steps occur sequentially onboard the 9000/300, in parallel to the 8510 as it collects the next dataset.
5. Convert the trace dataset into their logarithmic magnitude forms [For transmission data] apply normalization for the reference antenna, positioned 1 meter away from the AUT
6. Comb through the reflection and transmission response curves, searching for the frequency point of corresponding maximum transmission and minimum reflection; store the values found
7. Advance the “Capture” counter value by 1
8. Append the processed trace data to their relevant plot windows
9. Refresh/update the info banner (below the plot windows) displaying both the current “Capture” number as well as the

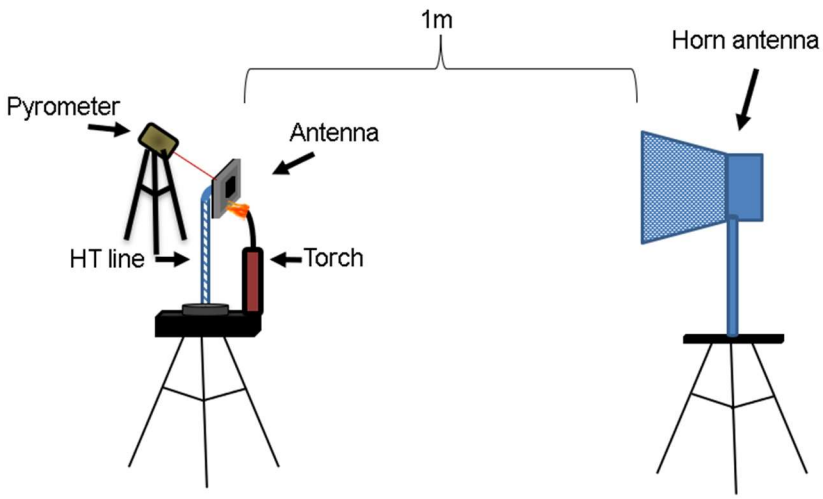
frequency/reflection-minimum/transmission-maximum that was found/stored in step 6

10. Print a hard copy of this updated banner line (for back-up redundancy) and, simultaneously, export the line to a modern PC via the RS-232 serial link
11. [End of cycle - Repeat beginning at Step 3]

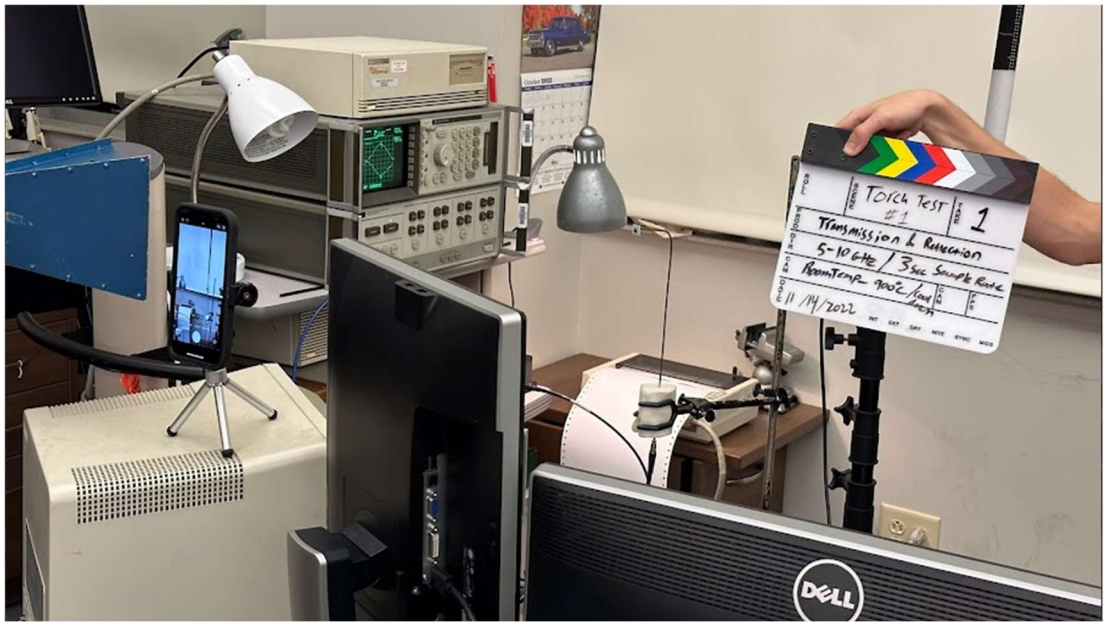
~Refer to the Appendix for complete program listing~

The test apparatus (Figure 4.16) consists of the retort stand with insulated clamp (used previously in the furnace tests) to which the bonded AUT/feedline is clamped. The AUT is connected to Port 1 of the 8510B. A reference horn antenna, connected to Port 2 of the 8510B, is positioned 1 meter away from the AUT at the same elevation. An Optris CT laser pyrometer, positioned tangential to the rear of the AUT, is pointed to a centered region of the AUT just above the feed line.

Two video cameras (Camera #1 and #2), synchronized via a clapper board, are utilized. Camera #1 is pointed at the AUT throughout the test, Camera #2 is pointed at the 9000/300's terminal screen to record the transmission and reflection plot fields and telemetry text banner as they update with each capture cycle. This banner consists of a "Capture #" counter, as well as the consolidated reflection/transmission extrema calculated for each capture and their respective frequencies.



a



b

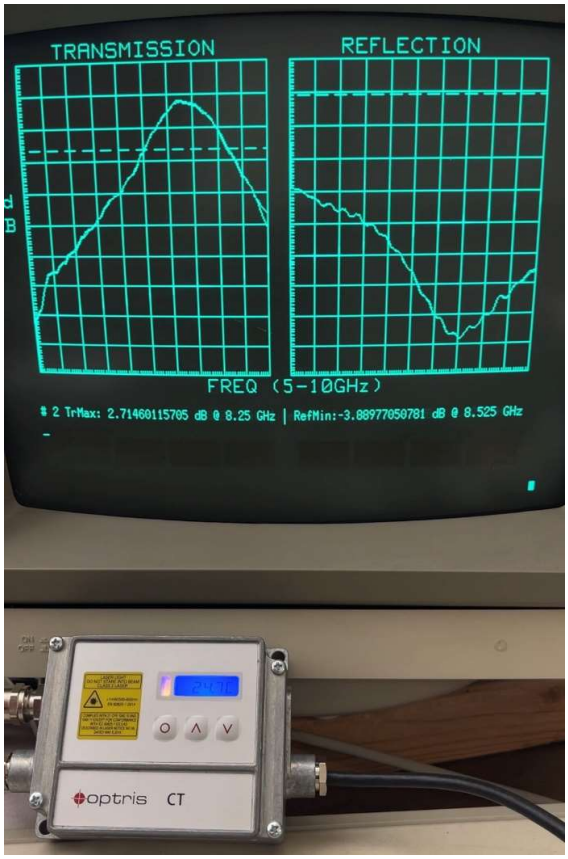
Figure 4.16: Torch Test Apparatus – Diagram (a), setup (b and c), Camera #1 view of AUT (d), Camera #2 view of HP 9000/300 terminal screen & pyrometer live LCD readout (e), view from pyrometer's positioning (f), preliminary wideband reflection and transmission sweep of AUT (g)



c

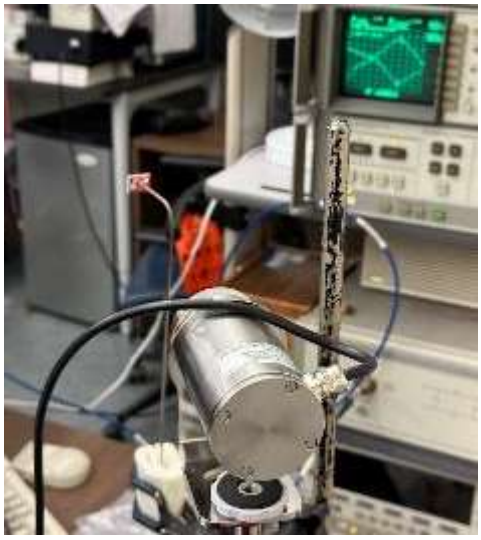


d

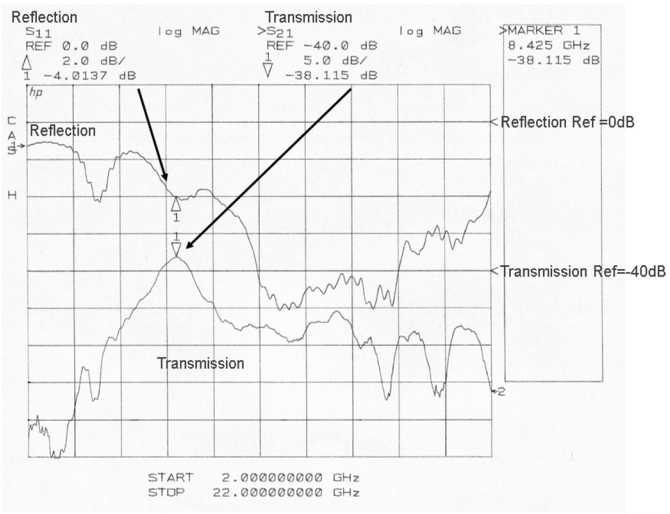


e

Figure 4.16 continued



f



g

Figure 4.16 continued

A Preliminary wide-band transmission/reflection measurement is performed. This is used to set the measurement and plot boundaries as displayed on the terminal. The real-time temperature LCD readout of the pyrometer is also in view of Camera #2. The pyrometer's readings-vs-time data is recorded separately onto a second PC. The video feeds provide for synchronization of all data collected during the test during post-processing upon completion.

4.5 Torch Test Procedure

With all equipment powered on and allowed at least one hour of warmup, an OSLT calibration is performed on the 8510, using the reference HT line for the Thru measurement. The test cables are then connected to both the AUT and reference horn, spaced one meter away. The pyrometer's aim is checked and aligned to where the AUT's rear ground plane resides squarely between the pyrometer's laser guides. A PuTTY session is launched on the PC to terminate and log the RS-232 null-modem connection with the 9000/300.

Camera #1 and #2 are initially positioned side-by-side, both pointing towards the same area. To begin the test, recording is initiated on the cameras, a clapper board is held in clear view of both and closed. This provides a frame synchronization marker for post-processing, as the cameras' recordings are not halted until after the test concludes. Camera #1 is repositioned

to focus on the AUT from the front. Camera #2 is relocated (still recording) to face the 9000/300's terminal screen and pyrometer LCD readout. The HP BASIC program is started and allowed to initialize the system and stabilize into its cyclical capture sequence. The pyrometer's bulk temperature logging program is started, noting the capture # displayed at the moment of commencement. The apparatus is now considered "live", and the test may proceed.

Following the lapse of multiple "baseline" captures with all logging and recording systems active, the MAPP torch was ignited and held tangentially-broadside to the AUT, such that the ~8in flame is allowed to reach and evenly flow across the antenna face, while preventing the metal nozzle and tank body from obstructing and/or imposing upon AUT and its line-of-sight signal path to the reference horn. The torch would be maintained in this orientation while the pyrometer's live LCD readout is monitored. Once the 900°C threshold is crossed, the torch is promptly removed and extinguished. All systems continue to log/record as the AUT is allowed to air-cool back down to room temperature, at which time, the equipment is halted in reverse-order from setup sequence; cessation of the cameras' recordings now held until last in the sequence.

CHAPTER V

RESULTS AND DISCUSSION

5.1 Color Commentary

Upon completion of the test, both video files were imported into Movavi Video Editor where the footage was arranged side-by-side and synchronized for timing. Portions of each cameras' field of view (specifically the Capture # and pyrometer live temperature readout) were duplicated, enlarged, and placed in the middle of the frame to provide concise real-time telemetry. The resulting unified clip facilitates a detailed analysis of the AUT's behavior throughout the progression of the test.

(Refer to figures 5.1a-m) The torch was applied to the AUT beginning at capture #20. The AUT reached 909.1°C by capture #34, 37 seconds later. The AUT returned to room temperature at capture #150, taking 5 minutes 3 seconds to air cool. During the heat cycle, the AUT's S21 transmission parameter appeared to gradually decrease as the higher end of the temperature range was approached, and then increase again during the cooldown, setting at approximately the same magnitude as it began with.

Its S11 reflection parameter initially presented a comparatively gradual increase; appearing to inversely track its S21 counterpart. At capture #28 (649.7°C), however, the reflections plateaued, and the resonance instead began to flatten out. At capture #33 (849.4°C), the reflections began dropping

rapidly, reaching its lowest point at capture #38; during the cooldown phase, when the AUT had returned to 603.8°C. The reflections quickly increased again – resonance dip becoming prominent again by capture #49, AUT cooled to 247.9°C. The AUT would remain with this same S11 response curve until capture #72 (89.9°C) when it would again begin to gradually drop until capture #138 (28.9°C) when it finally stabilized.

Event log (with respect to figure 5.1 parts):

a) Capture #20
   - Baseline room temperature – 24.8°C

b) Capture #28
   - 649.7°C
   - Transmission and Reflection response curves drift in tandem
   - Plasma begins to form around inner conductor of feedline (protruding out from patch face)

c) Capture #29
   - 664.8°C
   - Transmission realized gain drops below 0dBi

d) Capture #32
   - 801.2°C
   - Transmission curve continues steady drift
   - Reflection curve holds at same magnitude from capture #28, shape of curve flattens out instead.

e) Capture #33

- 836.3°C
- Reflection curve begins to drop sharply with its new, flatter shape

f) Capture #34

- Maximum Temperature Reached – 909.1°C
- Entire face of AUT enveloped in plasma
- Transmission realized gain maximum: -1.93dBi @7.8GHz
- Reflection resonance minimum: -4.06dB @9.475GHz (response curve fell below plot window range boundary)

g) Capture #35

- First complete cool-down capture - 839.9°C
- Reflection curve rebounds into plot window
  - Minimum: -4.34dB @9.475GHZ
- Transmission begins increasing
  - Realized gain maximum: -1.57dBi @8.175GHz

h) Capture #38

- 603.8°C
- Reflection curve rapidly drops (second occurrence)
- Transmission Realized gain becomes positive again
  - 0.68dBi @8.2GHz

i) Capture #39

- 547.5°C

- Reflection curve rebounds (second occurrence), returns to prominent dip-shape as it had in Capture #29 and prior
    - Minimum resonance: -4.81dB @8.525GHz

j) Capture #49

- 247.9°C
- Transmission and Reflection response curves gradually increase in unison

k) Capture #72

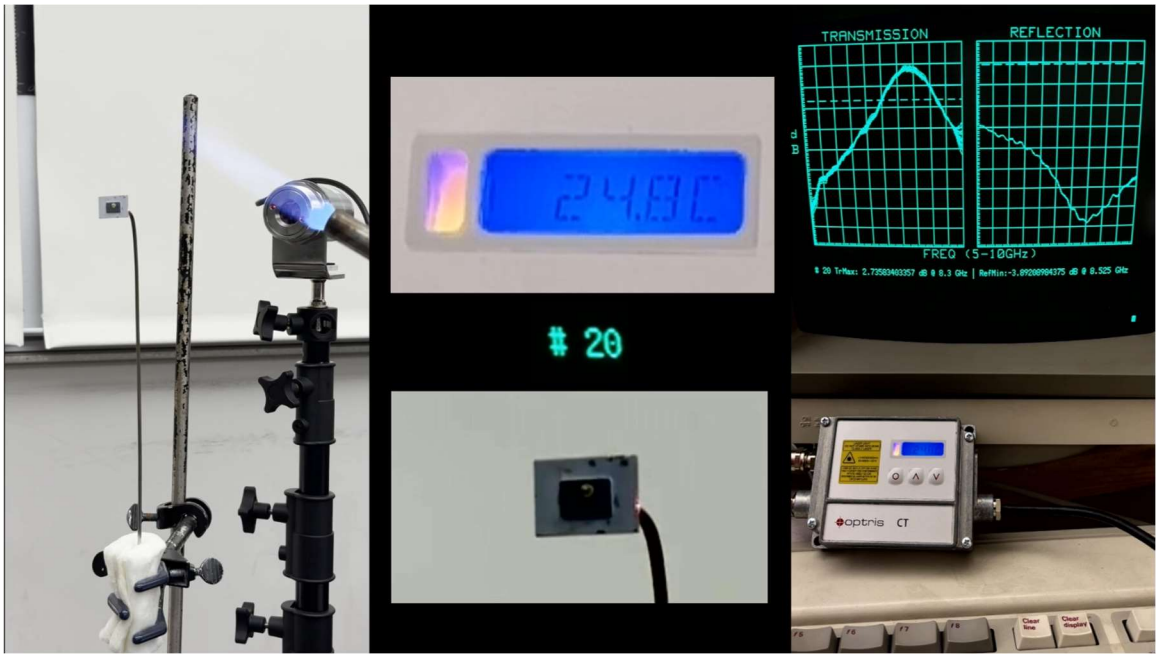
- 89.9°C
- Transmission response continues positive drift
- Reflection response begins drifting negative in tandem with increased transmission

l) Capture #138

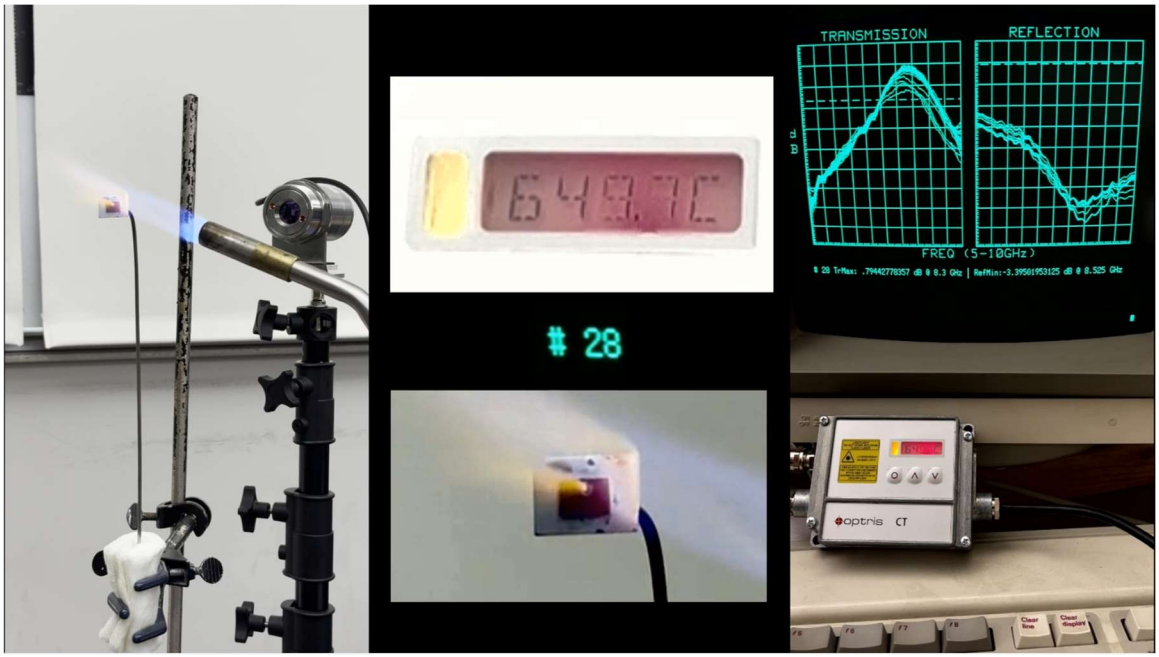
- 28.9°C
- Transmission and reflection curves stabilize

m) Capture #150

- Final Measurement: 27.2°C
- Transmission maximum realized gain: 1.85dBi @8.275GHz
- Reflection resonance minimum: -4.86dB @8.525GHz

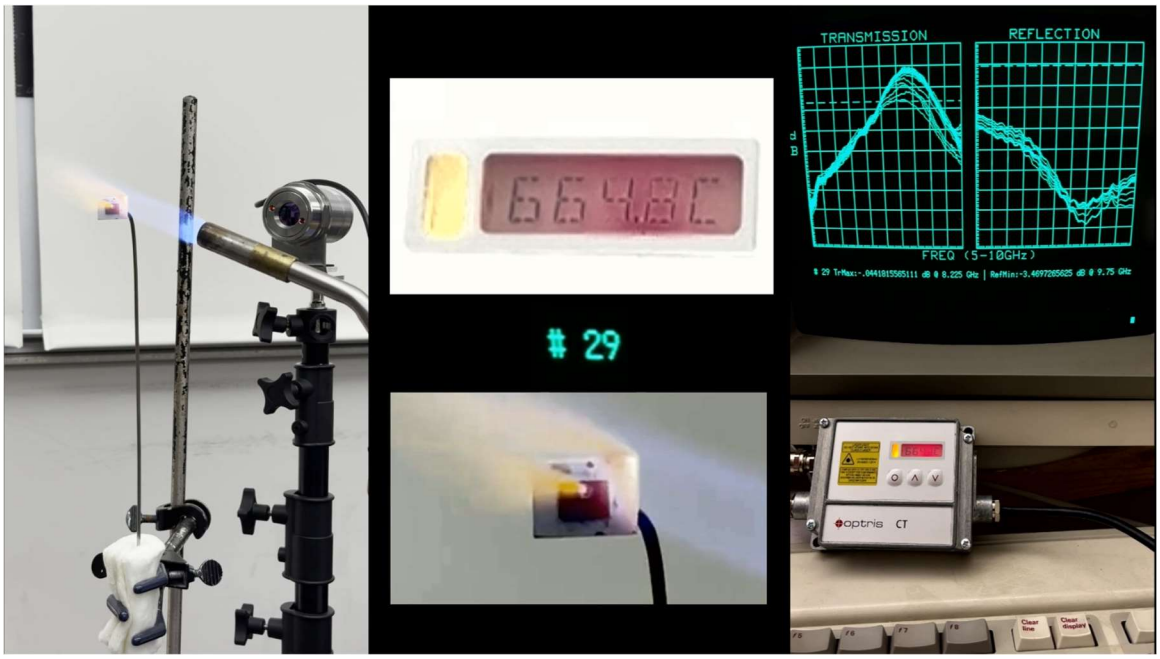


a

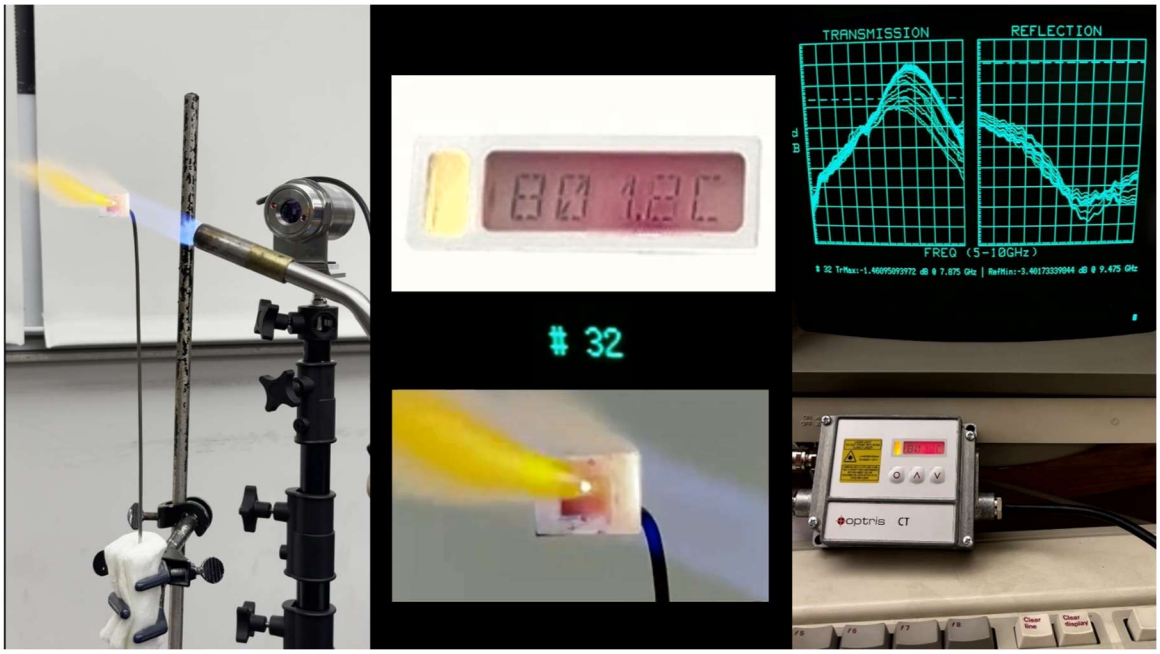


b

Figure 5.1(a-m): Unified video clip of torch test – screen captures of key events throughout the experiment. Camera #1 full view (left), Camera #2 full view (right), pyrometer live temperature readout close-up (top), AUT close-up (bottom), Capture # readout (center)

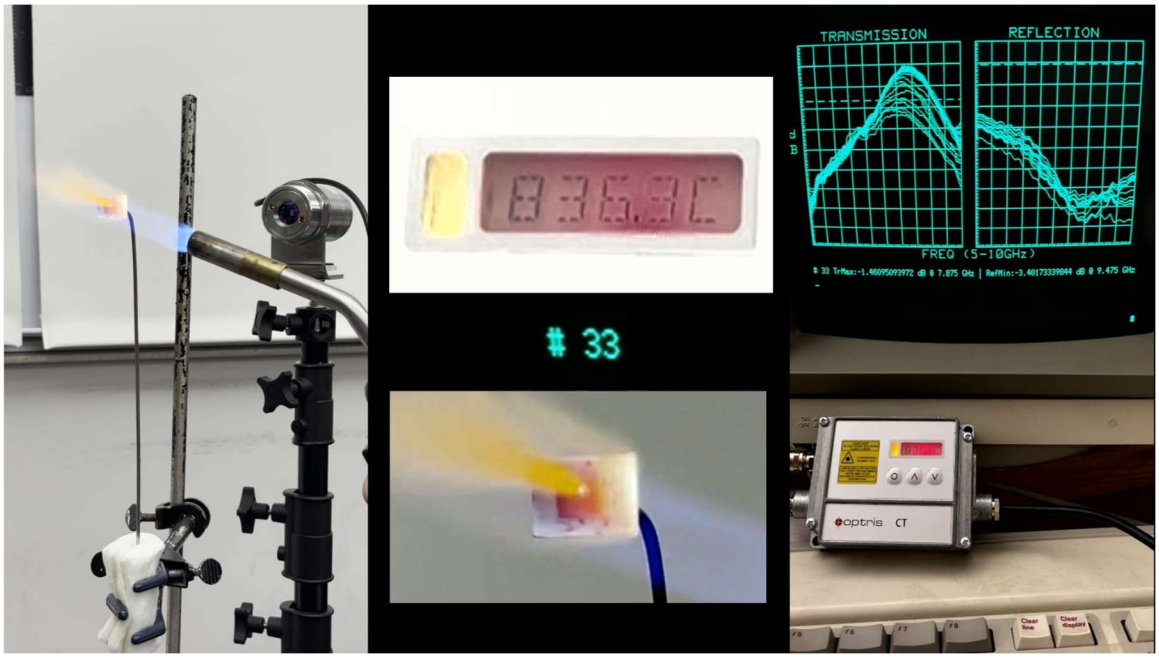


c

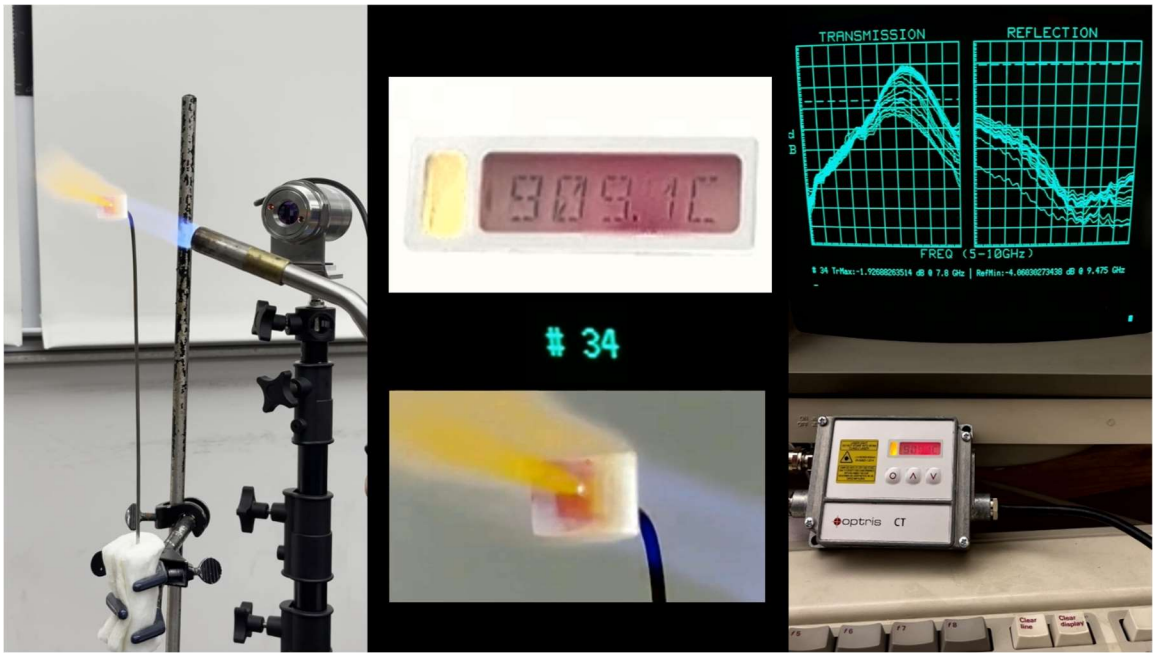


d

Figure 5.1 continued

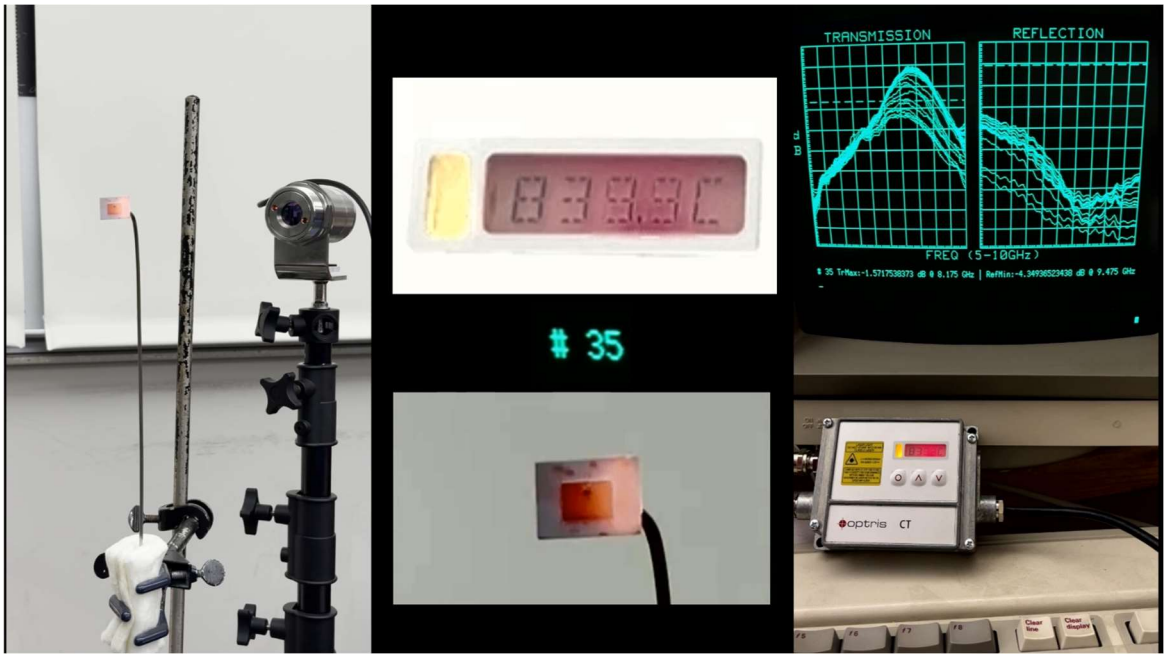


e

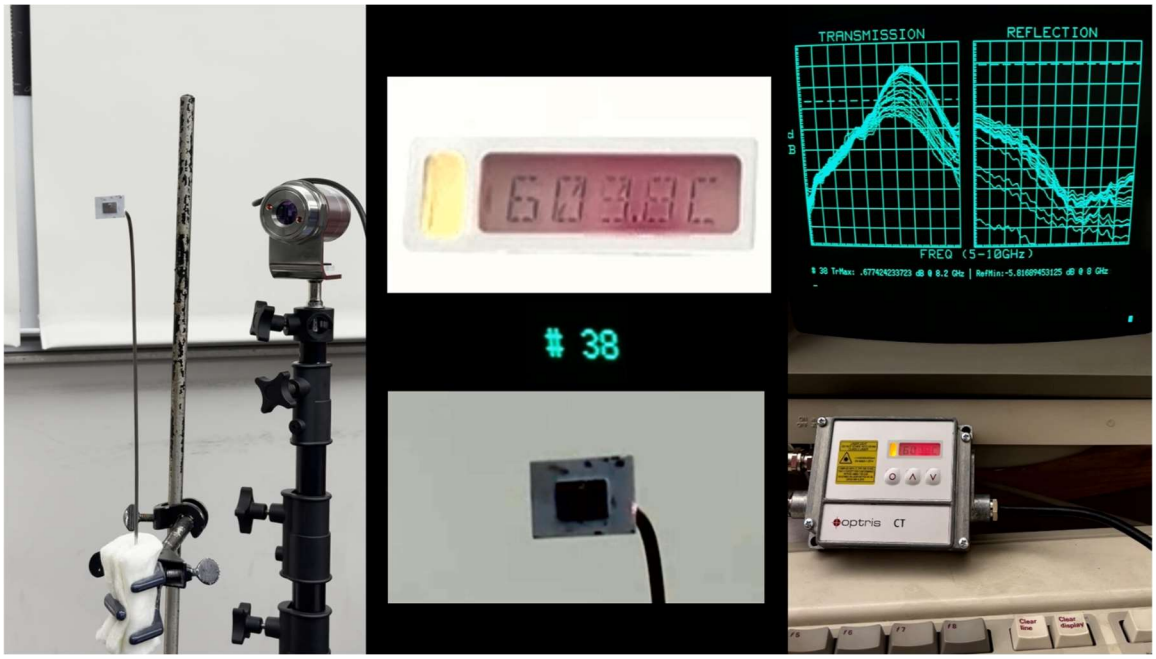


f

Figure 5.1 continued

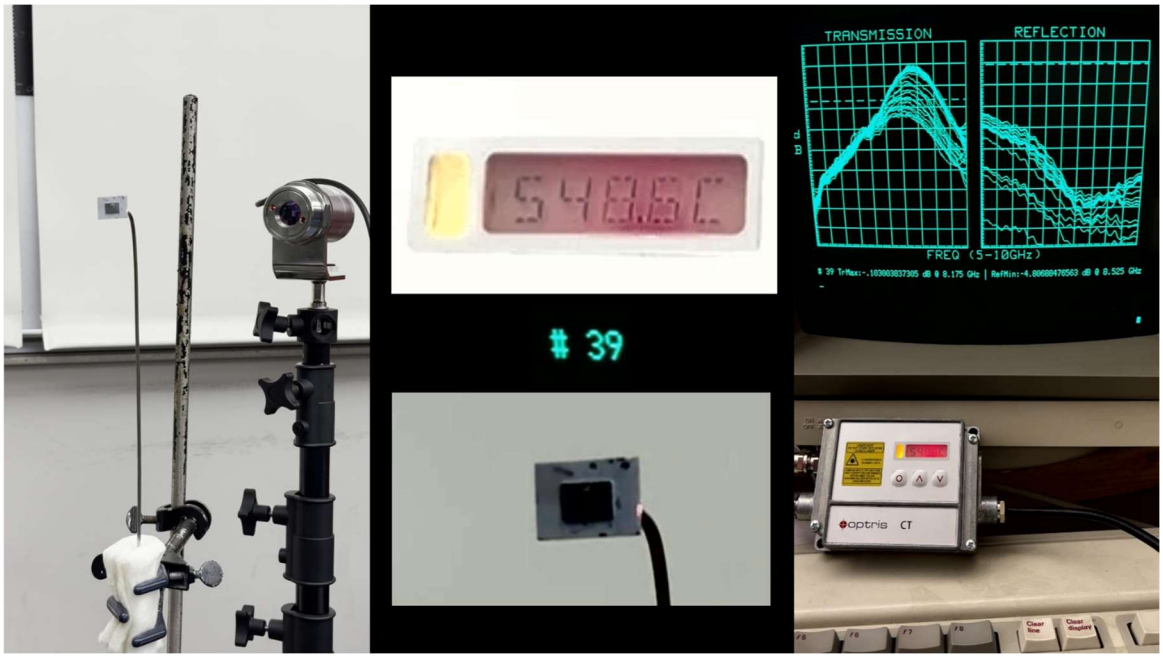


g

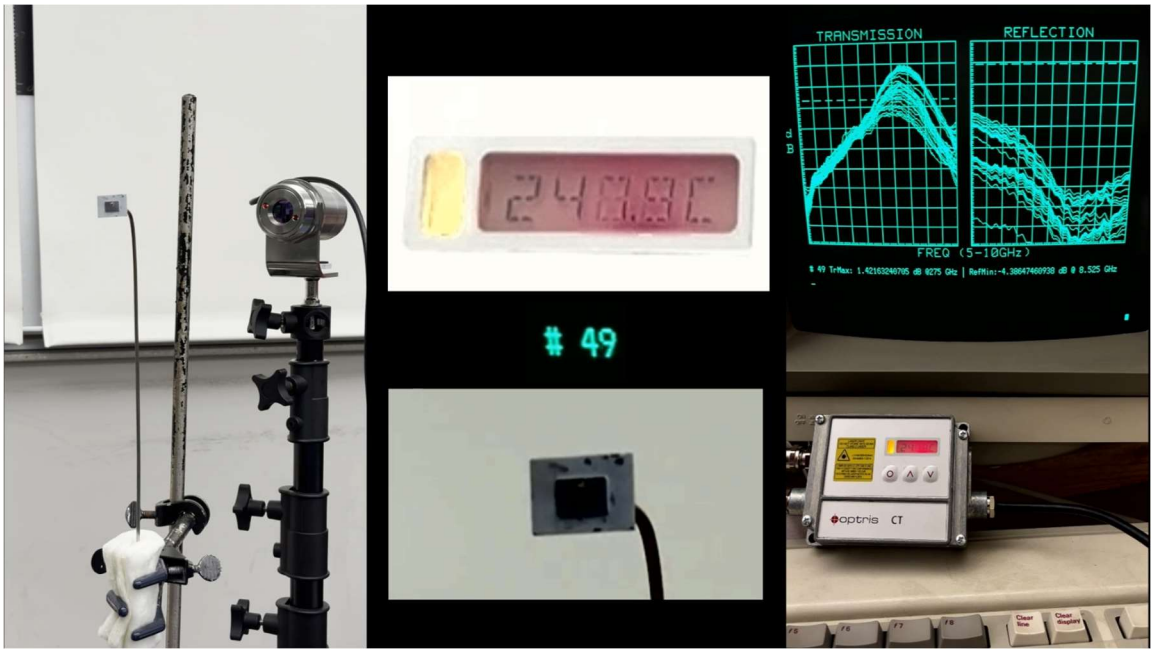


h

Figure 5.1 continued

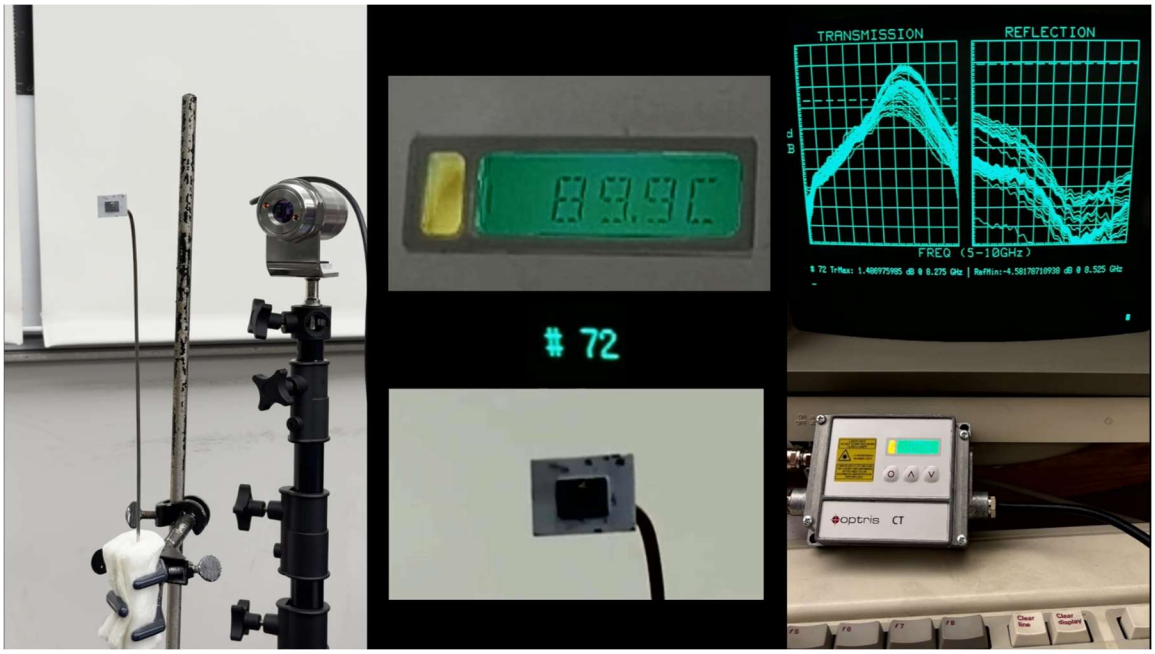


i

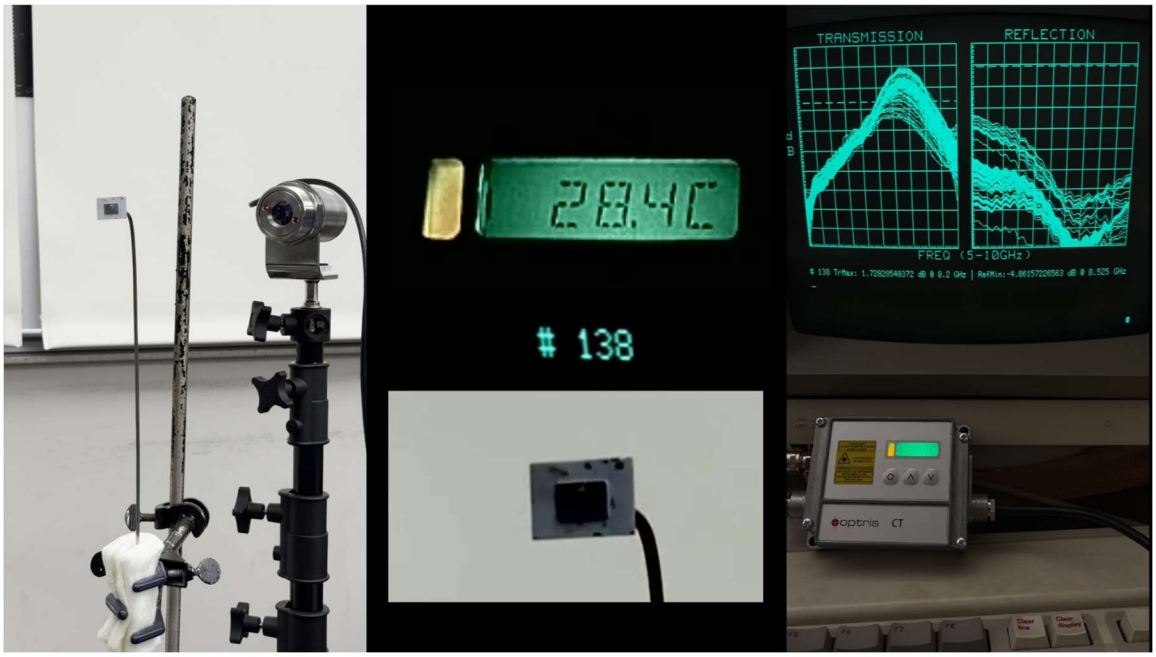


j

Figure 5.1 continued

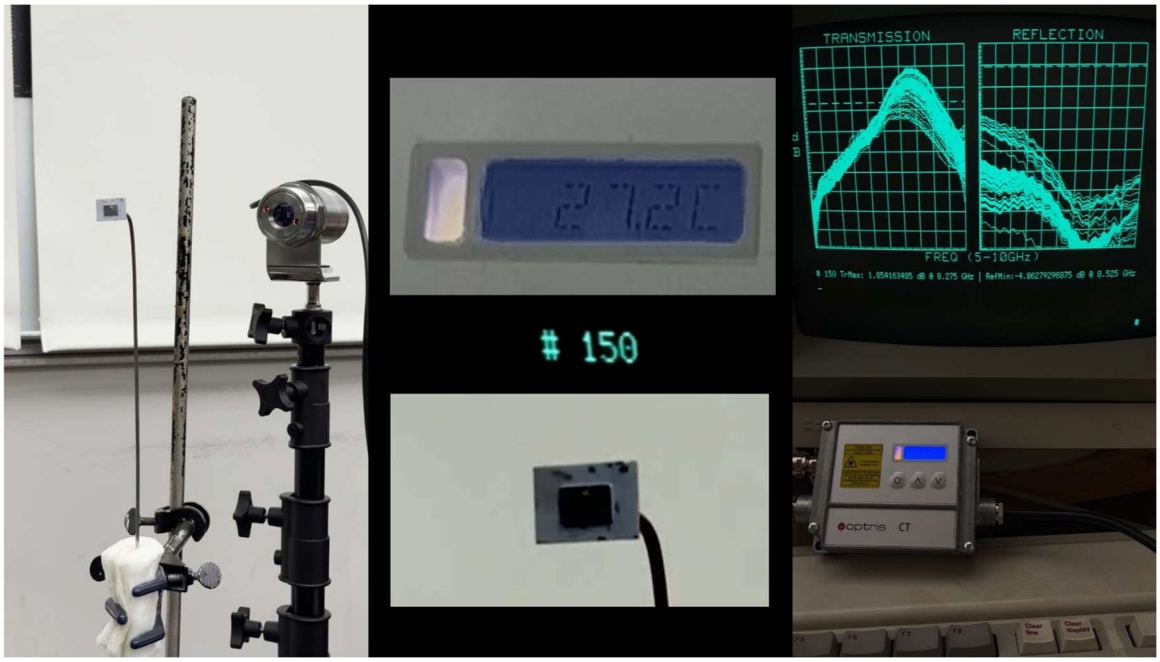


k



l

Figure 5.1 continued



m

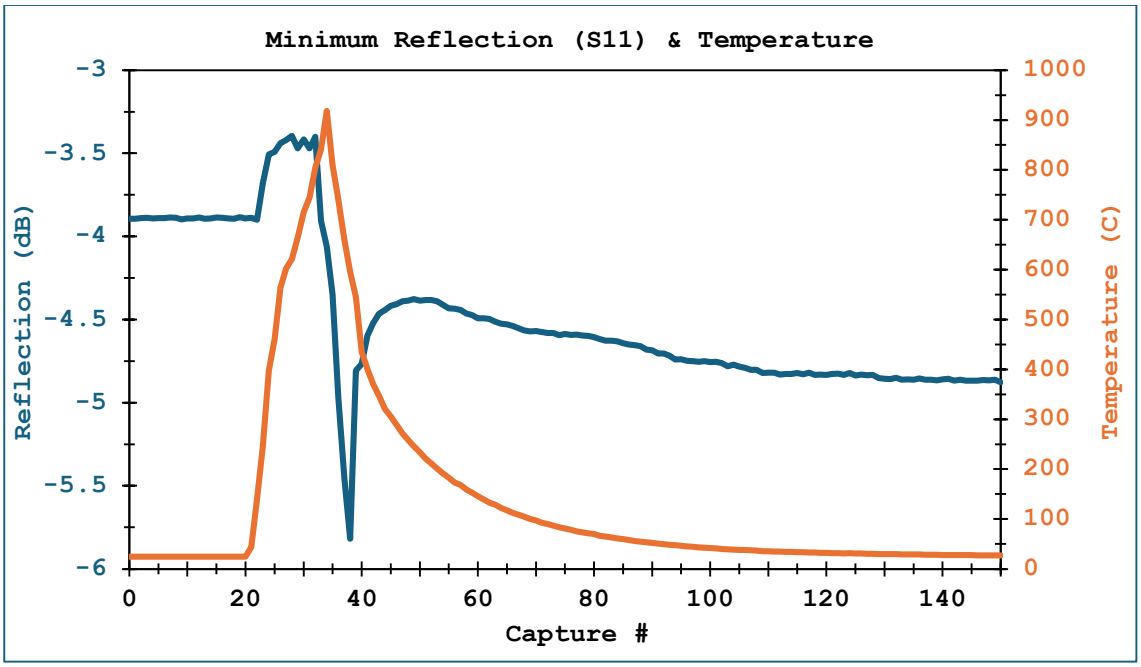
Figure 5.1 continued

5.2 Consolidated results analysis and conclusion

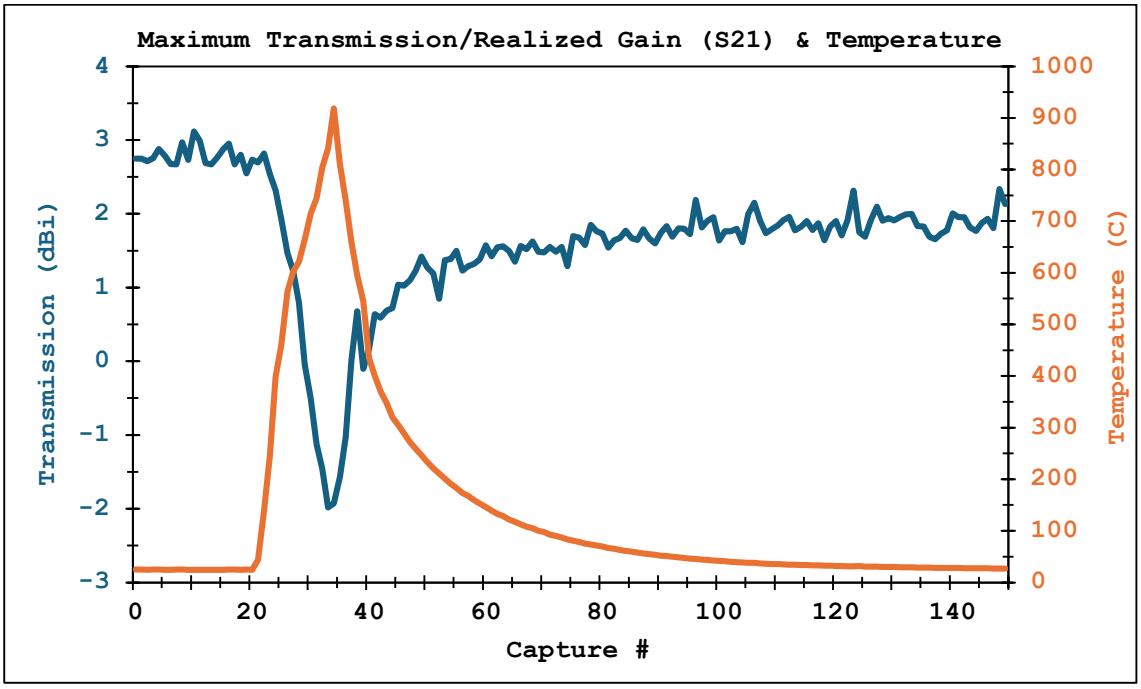
The condensed transmission-maximum, reflection-minimum, and corresponding frequency values determined for each capture (displayed as a continually updating text banner below the response plot windows on the HP 9000/300's terminal screen), were converted into a .csv format and transferred to a modern PC over an RS-232 null-modem connection (using PuTTY on the PC-side) during each capture cycle. This data may be compared with the Pyrometer's independently logged bulk temperature data, imported following the test's conclusion and matched to the corresponding capture # with the aid of the video footage. (Refer to Figure 5.2)

As the observed live telemetry readings indicated, the AUT's performance metrics exhibited pronounced deviation and degradation at temperatures in excess of 600°C. This behavior was certainly not unexpected; The distinctive downward shift in the AUT's nominal operating frequency, in direct momentary correlation to its temperature when beyond this apparent 600°C threshold, is a plainly anticipatable characteristic product of an antenna undergoing non-negligible amounts of thermal expansion and contraction.

A multitude of external contributing factors, both directly observed and of highly probable nature, account for much of the AUT's considerably diminished gain and wide variability of return loss experienced during the test. During the heating phase, a

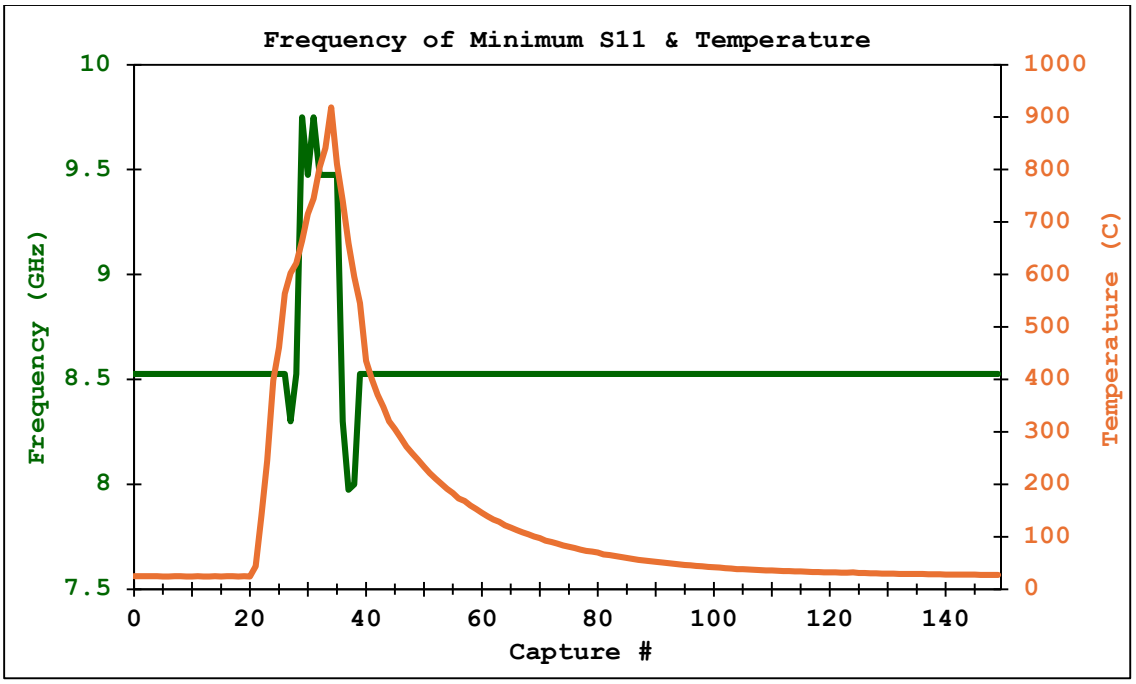


a

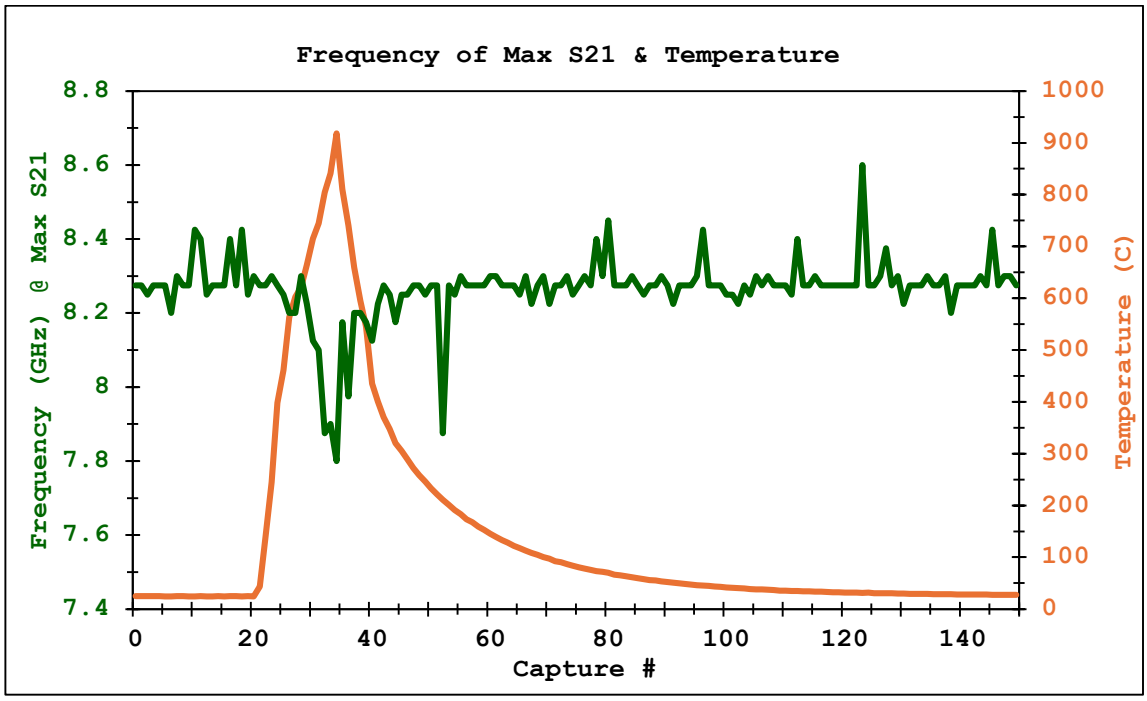


b

Figure 5.2: Consolidated telemetry extrema of return loss (a), realized gain (b), corresponding frequency of extrema (c and d respectively), and measured temperature of AUT (all graphs); versus capture #



c



d

Figure 5.2 continued

plasma trail, yellow in color, quickly formed across the face of the AUT. Initially localized as a faint, narrow, tail-like streak originating from the prevailing tip of the inner conductor's junction point with the patch, it gradually increased in coverage and intensity in unison with the AUT's temperature until the entirety of the antenna was engulfed. This thermionic cloud, notoriously reflective to RF and the historic culprit behind the ubiquitous "blackout period" experienced by nearly all spacecraft during reentry, potentially acted as a shield between the AUT and reference horn in a similar manner. (It should be stated that the premise of combating the plasma shield phenomenon directly is decisively outside the scope of this thesis.)

The heating method itself is also not immune from accountability. Considering that a torch is ultimately a stream of hot combustion products; particularly carbon and water, in addition to it not being a truly representative composition of the earth's atmosphere, these combustion products specifically may have potentially exacerbated the antenna's degradation as well. Some carbon exhaust particulates, when deposited randomly onto the AUT, could potentially change the effective shape of the resonant patch. Water condensate by itself can affect the dielectric properties of the antenna, however, when water is exposed to sufficiently high energy, it can dissociate into hydrogen and oxygen; the latter of which being the root detractor surrounding the furnace tests, and the primary motive behind the

torch test. While the likelihood is low of this specific means to which the carbon layers might be subjugated to undergo oxidation during the heating phase of the torch test, this potential should not go unacknowledged.

Unlike the actual manner in which heating occurs during hypersonic transit; friction generated between the exterior surface of the transiting vessel against the stationary (relatively-speaking) atmosphere around it, in this test, the torch method relies on the transfer/conduction of heat into the surface from an already superheated atmosphere. As stated in chapter 4, a MAPP torch burns at roughly 2925°C. While that is an appealing specification for selecting a method to rapidly heat an object, it also means it can cause portions of the object that have a higher thermal conductivity to heat up at a faster rate than others; namely, the protruding section of feedline as connected to the patch element. This could potentially have caused both the inner conductor and silver epoxy to inadvertently become heated beyond their manufacturer's ratings. It could just as likely have caused either to undergo thermal expansion at too dissimilar a rate, leading to fractures or severance of the feedline from the AUT.

Either or both scenarios might account for the erratic behavior of the reflection response curve observed throughout the progression of the test, seemingly independent of the transmission response curve, of which behaved relatively linear.

There exists a strong possibility that at some point between captures #33 and #39, the patch and feedline briefly became electrically disconnected, then later reconnected during cooldown. Transmission (albeit, diminished) would nevertheless be possible during such a scenario as the test signal could still air-couple through the resulting gap. This hypothesis is further evidenced by that of the continued asymmetric drift of the reflection response curve throughout the remainder of the cooldown phase.

Overall, the AUT did appear to "recover" (functionally speaking) from this intensive heat cycle, however, a seemingly permanent diminishment of gain is discernible. Comparing the average gain of the first 20 "baseline" captures taken prior to heating (2.787dBi), to that of the final 20 captures following cooldown (1.893dBi), the AUT suffered a net loss of 0.893dBi, or 9.773% decrease in gain performance as a result of the heat cycle.

With the primary overarching objective being to determine the viability of co-fired pre-ceramic polymers, to be used in place of conventional metal and insulative substrate materials in the creation of functional antennas, constructed via a novel 3D printing technique, that are thermally robust to the magnitude of temperatures typically experienced during hypersonic transit. The findings, as outlined above, point favorably to such viability.

Chapter VI

Conclusion

6.1 Summary

The objective of this thesis was to examine the potential of novel polymer derived ceramic formulations, and novel 3D printing technique, to create thermally robust antennas for use in hypersonic environments. Given the novelty of both materials and manufacturing technique, the approach to this endeavor was grounded in “first principles”.

Chapter I presented essential background material concerning the fundamental considerations required for incorporating antennas into airframe structures, provided a basic overview of hypersonics with an emphasis on the harsh thermal characteristics involved, and the foundational premise of this thesis. The underlying principles and theory concerning dielectric characterization were presented In Chapter II. Comparisons and evaluations of standard characterization techniques were also discussed.

Chapter III introduces the novel PDC formulations and details the manufacturing process. Included are the evaluation and characterization of sample blocks of each material, sized to determine the general capabilities and limits of the prototype 3D printer and manufacturing system. A generalized set of antenna design parameters were established based on those preliminary findings. Prototyping, as well as design, measurement, and manufacturing refinements are also detailed in this chapter.

In Chapter IV, the logistical considerations and challenges concerning high temperature antenna testing were discussed. A testing strategy was formulated, result1ng from a series of preliminary tests, in an effort to optimally replicate the environments associated with hypersonic flight, while maintaining a sufficiently acceptable degree of confidence in the validity of data gathered. The results of the preliminary tests are presented and discussed in this chapter, while the results of the main test are detailed and analyzed in Chapter V.

6.2 Conclusions

The prospects of using 3D printable PDC formulations to create antenna structures suitable for hypersonic applications have been proven to be valid and promising, as this thesis reports. While further refinement and testing is in order prior to any real-world implementation, the premise that a functional antenna can be 3D printed in complementary PDC formulations and can operate at exceedingly-high temperatures holds true.

The experimental results indicate that, for the specific PDC formulations and manufacturing equipment used, the apparent maximum sustainable operating temperature is approximately 700°C, in a terrestrial-level atmospheric composition. This limit is primarily attributed to the effects of oxidation, as discussed in Chapter IV, due to the limitations in equipment used to perform the high temperature tests; specifically, the inability to control the atmospheric composition within the testing apparatus, and the maximum temperature ratings of both the silver epoxy and high temperature feed lines (as published by the manufacturers)

having been grazed, the absolute-maximum sustainable operating temperature of these antennas remains inconclusive. It can be hypothesized, however, that this metric could potentially reach, or perhaps exceed 1500°C, as that was the temperature sustained during the pyrolization phase of manufacturing (in a Nitrogen-purged tubular furnace).

Carbon migration complicated the design process and contributed to the overall lossiness observed in each prototype iteration. Nevertheless, refinements implemented in successive iterations managed to greatly mitigate the effects and significantly narrowed the margins of inconsistency. Further refinement would likely bring the antennas' performance closer to their theoretical specifications, particularly through the implementation of pre-emphasis measures applied to the design prior to printing. Complete elimination of carbon migration is beyond the scope of this thesis.

The ability to 3D print ceramic structures alone certainly posits an assortment of lucrative applications and opportunities in, but not limited to, hypersonics. The additional ability to embed electrically conductive formulations, that are otherwise materialistically identical such to produce a virtually homogeneous finished product, has great potential to revolutionize the construction and technological capabilities of hypersonic flight vehicles.

6.3 Future Works

The next steps of this work would likely entail the design and integration of feed lines using these PDCs and 3D printing

technique. This would greatly enhance the reliability of coupling between the antenna and that of conventional RF hardware and devices not rated for such extreme environments. In a similar vein, move on to explore other types of antenna structures that might pose lesser effects and/or sensitivity to carbon migration. Keeping within the spirit of the premise of this work, the true "next step” would be to test these prototype antennas in real hypersonic environments; either in a capable wind tunnel, such as the NASA Ames Arc Jet Complex, or (ideally) affixed to a sufficiently powerful sounding rocket.

REFERENCES

[1] Keysight, Appl. Note 5989-2589: “Basics of Measuring the Dielectric Properties of Materials”, (2020).

[2] Hewlett-Packard, Appl. Note AN-221A: “Automating the HP 8410B Microwave Network Analyzer”, (June 1980).

[3] Hewlett-Packard, HP 8503A S-Parameter Test Set Operating and Service Manual pp.3-10, (August 1978).

[4] Hewlett-Packard, HP 8510 Network Analyzer Operating and Service Manual pp.1-14, (April 1984).

APPENDIX

HP BASIC Controller Program Listing:

```
10    OPTION BASE 0
20    DIM Data(200,1)
21    DIM Data2(200,1)
30    DIM Formatted_data(200,1)
40    DIM Input$[80]
50    INTEGER Length,Error_number,Bytea,Byteb
60    REAL Freq,Real,Imag,Mag,Phase
70    DIM Freq_list(200),Mag_list(200),Phase_list(200)
80    ASSIGN @Nwa TO 716
90    ASSIGN @Nwa_data1 TO 716;FORMAT ON
100   ASSIGN @Nwa_data2 TO 716;FORMAT OFF
110   INTEGER Size,Preamble
120   ASSIGN @Nwa_systbus TO 717
130   ASSIGN @Nwa_systbusdaya TO 717;FORMAT ON
140   REMOTE 7
150   !ASSIGN @Nwa_printer TO 701
151   PRINTER IS 701
160   OUTPUT @Nwa;"DEBUON;"
170   OUTPUT @Nwa;"ENTO;"
180   REMOTE @Nwa
181   OUTPUT @Nwa;"FORM3;CHAN2;OUTPFORM;"
182   ENTER @Nwa_data2;Preamble;Size;Data(*)
260   OUTPUT 9;CHR$(12)
275   PRINT "              ********** TRANSMISSION TEST
**********"
276   PRINT "CAPTURE# NORM'D-MAX(dB, S21) TRANS FREQ
(GHz)|MIN REFL(dB, S11) REF
L FREQ (GHz)"
277   OUTPUT 9;"              ********** TRANSMISSION TEST
**********"
278   OUTPUT 9;"CAPTURE #   NORM'D MAX (dB, S21)  TRANS FREQ
(GHz)   MIN REFL (d
B, S11)   REF FREQ (GHz)"
280   Counter=1
1000  GINIT
1001  Refmin=0
1002  Refminfreq=0
1004  Trmax=0
1005  Trfreqmax=0
1006  Trmaxnorm=0
1007  DIM Prdat(4)
1010  PLOTTER IS CRT,"INTERNAL"
1013   CLEAR SCREEN
1020  GRAPHICS ON
```

```
1030  MOVE 10,95
1040  LABEL " TRANSMISSION         REFLECTION"
1050  MOVE 0,65
1060  Label$="dB"
1070  FOR I=1 TO 2
1080    LABEL Label$[I,I]
1090  NEXT I
1100  MOVE 45,25
1110  LABEL "FREQ (5-10GHz)"
1111  GOTO 1232
1120  VIEWPORT 5,60,30,95
1130  FRAME
1140  WINDOW 0,200,-56,-36
1150  AXES 2,.2,0,-56,10,10,3
1151  GRID 20,2,0,-56
1152  LINE TYPE 5
1154  PLOT 1,-41.3031703769
1155  PLOT 200,-41.3031703769
1156  LINE TYPE 1
1158  PLOT 200,-56
1159  PLOT 1,-56
1181  FOR X=1 TO 200
1182    PLOT X,Data(X,0)
1183  ! PLOT X,Data(X,1)
1184  NEXT X
1185  PLOT 200,-56
1186  PLOT 1,-56
1187  Trmax=Data(1,0)
1188  FOR S=1 TO 200
1189    IF Data(S,0)>Trmax THEN
1190       Trmax=Data(S,0)
1191       Trmaxfreq=5+.025*S
1192    END IF
1193  NEXT S
1194  Trmaxnorm=Trmax-20*(LGT(.3/(4*PI*Trmaxfreq)))-9.65
1195  VIEWPORT 65,120,30,95
1196  FRAME
1197  WINDOW 0,200,-4.5,.5
1198  AXES 2,.05,0,-4.5,10,10,3
1199  GRID 20,.5,0,-4.5
1200  LINE TYPE 5
1201  PLOT 0,-.05
1202  PLOT 200,-.05
1203  PLOT 0,-.05
1204  LINE TYPE 1
1205  FOR Y=1 TO 200
1206    PLOT Y,Data2(Y,0)
1207  NEXT Y
1208  PLOT 200,-4.5
1209  PLOT 0,-4.5
```

```
1211  Refmin=Data2(1,0)
1212  FOR Z=1 TO 200
1213     IF Data2(Z,0)<Refmin THEN
1214        Refmin=Data2(Z,0)
1215        Refminfreq=5+.025*Z
1216     END IF
1217  NEXT Z
1218  Prdat(0)=Counter
1219  Prdat(1)=Trmaxnorm
1220  Prdat(2)=Trmaxfreq
1221  Prdat(3)=Refmin
1222  Prdat(4)=Refminfreq
1224  !PRINT "MAX= ";Trmax;" dB @";Trmaxfreq;" GHz"
1225  DISP "#";Counter;"TrMax:";Trmaxnorm;"dB
@";Trmaxfreq;"GHz | RefMin:";Refmi
n;"dB @";Refminfreq;"GHz"
1226  !PRINT "    ";Counter;"
";Trmaxnorm;"                ";
Trmaxfreq
1227  PRINT Prdat(*)
1228  OUTPUT 9;Prdat(*)
1230  !BEEP 1000,.01
1231  Counter=Counter+1
1232  REMOTE @Nwa
1233  OUTPUT @Nwa;"CHAN2;NUMG1;OUTPFORM;"
1234  ENTER @Nwa_data2;Preamble,Size,Data(*)
1235  OUTPUT @Nwa;"CHAN1,OUTPFORM;"
1236  ENTER @Nwa_data2;Preamble,Size,Data2(*)
1237  LOCAL @Nwa
1238  GOTO 1120
1239  GOTO 400
9999 !CLEAR SCREEN
10000 OUTPUT @Nwa;"DEBUOFF;"
10001 LOCAL @Nwa
10005 END
```

VITA

Peter Jessup Alley was born in Kingsport, Tennessee, on June 30, 1994. He attended Dobyns-Bennett High School and graduated in 2013. He received his Bachelor of Science degree In Electrical Engineering from the University of Tennessee in 2019. He then continued at the institution in pursuit of his master's degree, joining the microwave research group. His life-long passion for analog electronics stems from his hobby of collecting and restoring vintage tube electronics, particularly televisions.